Graphene and Two-Dimensional Transition Metal Dichalcogenide Materials for Energy-Related Applications

Gyeong Sook Bang and Sung-Yool Choi

Abstract The energy problem is one of the most challenging issues in the twenty-first century. Many energy applications for portable electronics, electric vehicles, spacecraft, and renewable energy are under extensive investigation worldwide. New alternative energy with renewable energy devices are competitive with fossil fuels. To develop the advanced energy storage and harvesting/conversion system, renewable energy nanomaterials are in high demand. Two-dimensional nanomaterials composed of graphene and two-dimensional transition-metal chalcogenides (2D-TMDs) have attracted a great deal of interest due to their unique properties. From the prospect of energy applications, graphene and 2D-TMD nanosheets have many interesting properties, such as large surface area, atomically thin sheet with high flexibility, and a wide range of electrical conductivity. Graphene has proved to be a good material for nanoscale devices used in energy harvesting/conversion and storage applications. Recently, 2D-TMDs are also attracting significant attention in many energy-related applications. In this chapter, we focus on the recent advances in graphene (including graphene oxide, GO) and 2D-TMD nanosheets research for energy devices: electrodes in solar cell, electrocatalysts or photocatalysts for fuel cell, electrodes in Li-ion battery, and electrodes for supercapacitors.

Keywords Graphene · Transition-metal dichalcogenides (TMDs) · Nanosheets · Solar cell · Fuel cell · Li-ion battery · Supercapacitor

G.S. Bang · S.-Y. Choi (✉)
School of Electrical Engineering, Graphene Research Center,
Korea Advanced Institute of Science and Technology, Daejeon, South Korea
e-mail: sungyool.choi@kaist.ac.kr

1 Introduction

The rapid development of better energy-related devices has generated some of the most important challenges in the twenty-first century. Extensive studies around the world have been focused on energy products such as portable electronics, electric vehicles, spacecraft, and renewable energy. Low cost, high efficiency, sustainable-energy devices are in high demand. As new alternative energy devices have become more competitive with fossil fuels, renewable energy nanomaterials for energy harvesting and energy storage are in high demand.

Two-dimensional (2D) nanomaterials composed of graphene and nanostructured transition-metal dichalcogenides (TMDs) have attracted a great deal of interest due to their unique properties. These make them good candidates for potential applications in electronic devices such as supercapacitors, light-emitting diodes, solar cells, fuel cells, piezoelectric nano-generators, and lithium-ion batteries.

When it comes to energy-related applications, graphene and 2D-TMD single-layers have many advantages: (1) atomic thickness for quantum confinement of charge carriers, (2) electrical properties that vary from those of metal to semiconductor to insulator, (3) good cycle stability and flexibility, (4) high catalytic activity, and (5) short path-lengths for electron transport. Moreover, 3D structures incorporating graphene and 2D-TMDs are more attractive electrode materials in applications related to renewable energy. In particular, their properties related to the versatile electrical conductivity and their huge surface area are useful in enhancing the performance of energy devices.

Since its discovery in 2004 [1] graphene has demonstrated its role in enabling rapid advances in energy technologies for high-performance energy devices. Moreover, 2D-graphene has proven a good material for nanoscale devices used in energy harvesting, energy conversion, and storage applications. Recently, layered TMD materials (e.g., MoS_2, WS_2, $MoSe_2$, and WSe_2) are attracting significant attention in many energy-related applications. Their crystal structure varies from hexagonal (MoS_2, WS_2) to ortho-rhombic ($MoTe_2$, WTe_2). Nanosheets of 2D-TMDs possess remarkably different electronic properties than those of bulk TMDs, which can exhibit either semiconductor or metallic behavior depending on their elemental composition and method of synthesis. The optical properties of 2D-TMD nanosheets make them potentially useful for energy harvesting and conversion materials in solar cells, photoelectrochemical cells, and photo-fuel cells. Their graphene-like layer can also be used for energy storage devices such as Li-ion batteries and supercapacitors.

Here, we focus on the recent advances on graphene (including graphene oxide, GO) and 2D-TMD nanosheets for use in energy devices: specifically, electrodes in solar cells, electrocatalysts and photocatalysts for fuel cell, electrodes in Li-ion batteries, and electrodes for supercapacitors.

2 Electronic Structure and Synthesis of 2D Materials

2.1 Electronic Structure

Graphene This substance can be made to assume the form of single-atom-thick, 2D single-layer of sp^2 hybridized carbon atoms in a honeycomb crystal lattice. In this form, it has unique structure and properties. These include rich electronic states (excellent conductivity of 10^6 S cm^{-1} and thermal conductivity of 5000 W m^{-1} K^{-1}), good mechanical properties (Young's modulus of 1.0 TPa), large surface area (2630 m^2 g^{-1}), optical absorbance of ~2.3 % for visible light, high transparency, high flexibility, and easy modification using organic and inorganic molecules. Detailed descriptions of the overall properties of graphene have been published elsewhere [2–7].

Because it possesses these superior properties, graphene is still being studied intensely as an attractive candidate for many energy-related applications [8–21].

2D-TMDs Atomically thin 2D-TMDs (6.5 Å thick) have received much attention in recent years, because they are naturally abundant, have unique properties and form semiconductors with various bandgaps [6, 22]. Layered TMDs are materials with the formula MX_2, where M is a transition metal from Group-4 to Group-7 and X is a chalcogen of S, Se, or Te. Their structures are formed of covalently bonded X-M-X single-layers that interact by van der Waals forces (Fig. 1a). Each single layer consists of two X atom layers and a layer of metal atom sandwiched between two layers of chalcogens. Transition metal atoms provide four electrons to fill the bonding states of MX_2, oxidation states of +4 for metal atoms, and oxidation states of −2 for chalcogen atoms. The d-electron count of the transition metal relates to the MX_2 phase. The metal atoms of MX_2 can have either
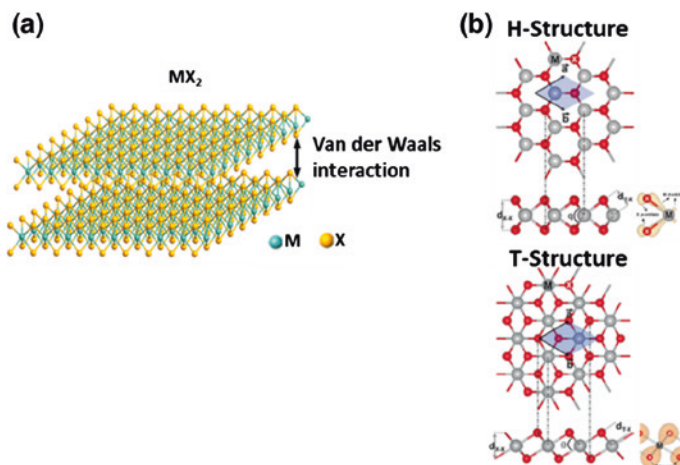

Fig. 1 **a** Layered MX_2 structure. **b** Atomic structure for MX_2 in the H and T structure. (Reproduced with permission from Ataca et al. 2012 [24]. Copyright © 2012 American Chemical Society)

trigonal prismatic or octahedral coordination. Bulk MX_2 exhibits three different stacking-types: 1T (trigonal), 2H (hexagonal), and 3R (rhombohedral) [6, 23]. Group-6 bulk MX_2 is mostly of 2H structure, which is more stable than the 1T phase. Single-layer MX_2 is of only two types: 1H and 1T (Fig. 1b) [24]. Each M atom has six X atoms, and each X atom has three M atoms forming hybridization of the M d-orbital and X p-orbital. The change in symmetry induces changes in the electronic properties from semiconducting to metallic [25, 26]. Thus, MX_2 nanosheets have electronic properties from semiconducting to metallic, depending on their geometry, composition, thickness, and electron density. The phase transition from 2H to 1T can be induced by specific procedures.

The bandgap of MX_2 varies with a number of layers. Calculations using density functional theory (DFT) have shown that the MoX_2 and WX_2 materials can change from indirect-to-direct bandgaps, depending on the number of layers (Fig. 2) [6, 27–30]. Single-layer MX_2 is a direct bandgap semiconductor with bandgap energy of $1.2-2.1$ eV, whereas bulk MX_2 is an indirect bandgap semiconductor with bandgap energy of $1.0-1.4$ eV. The electronic properties of MX_2 are summarized in Table 1.

Contrary to zero-bandgap graphene, single-layer 2D MX_2 sheets are semiconductors with a small direct-bandgap, which is a useful material for a wide range of applications (e.g., field effect transistors, energy harvesting/conversion devices, optoelectronics, and sensors). Transistors of single-layer MoS_2 using HfO_2, exhibited a mobility of 200 cm^2 V^{-1} s^{-1} [32]. Other properties shown are Young's
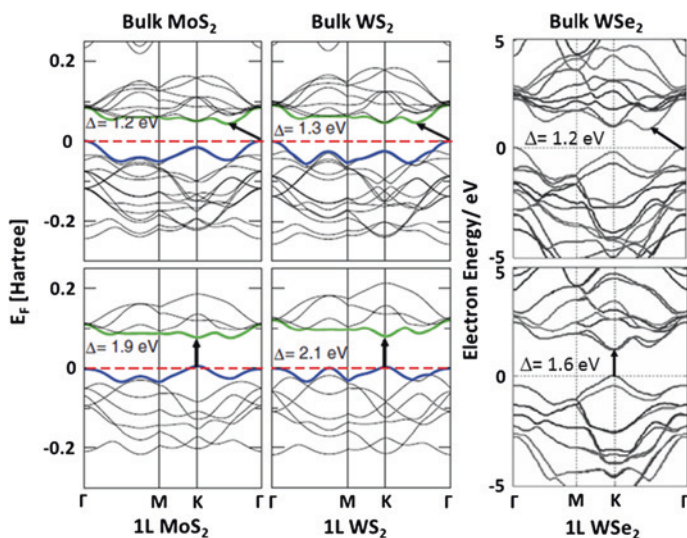

Fig. 2 Electronic band structures of bulk and single-layer MX_2. The *black arrows* are their band gaps. (Reproduced with permission from: (MoS_2, WS_2) Kuc et al. 2011 [28]. Copyright © 2011 American Physical Society. (WSe_2) Huang et al. 2014 [30]. Copyright © 2014 Royal Society of Chemistry)

Table 1 Electronic properties of MX$_2$ materials [6, 28, 30, 31]

Metal	X, chalcogen		
	S	Se	Te
Mo	Semiconductor	Semiconductor	Semiconductor
	Bulk: 1.2 eV	Bulk: 1.1 eV	Bulk: 1.0 eV
	1 L: 1.8–1.9 eV	1 L: 1.5–1.6 eV	1 L: 1.2 eV
W	Semiconductor	Semiconductor	Semiconductor
	Bulk: 1.4 eV	Bulk: 1.2 eV	Bulk:
	1 L: 1.9–2.1 eV	1 L: 1.6–1.7 eV	1 L: 1.2 eV

modulus of 270 ± 100 GPa for MoS$_2$ single-layer [33] and in-plane resistivity of 3–40 kΩ/sq [34] and 14–28 kΩ/sq [35] for micromechanical exfoliated MoS$_2$ and CVD-grown MoS$_2$, respectively. The direct-bandgap transition in single-layer MX$_2$ provide enhanced photoluminescence (PL) by quantum confinement effects. Moreover, MoS$_2$ single-layer exhibits optical-valley polarization [36, 37] and lesser stiffness than graphene [38]. The electronic band structure of 2D-MX$_2$ not only depends on the number of layers but also on the strain [27].

In summary, both graphene and 2D-MX$_2$ nanosheets have a great number of superior properties that make them attractive candidates for use in energy harvesting, energy conversion, and storage applications.

2.2 Synthesis Methods

Graphene and 2D-MX$_2$ can be obtained from a variety of methods including micromechanical exfoliation (also called scotch-tape method), chemical vapor deposition (CVD), and liquid-based exfoliation. Each preparation method results in products with particular structures and properties. Graphene and 2D-MX$_2$ processed using liquid-based-exfoliation and CVD methods have often been used in energy harvesting, conversion, and storage applications due to their large surface area and ease of mass production. [7, 39–48].

2.2.1 Micromechanical Exfoliation

Graphene become an important material after discovery through micromechanical exfoliation method by Novoselov et al. (2004) [1]. Micromechanical exfoliation is the best known method for obtaining high quality graphene. This method produces graphene from bulk crystals of layered graphite by repeated exfoliation using scotch tape [1, 49] (Fig. 3). Like graphene, a 2D-MX$_2$ single-layer can be exfoliated from bulk MX$_2$ crystal using scotch tape [50]. Other layered materials can also be exfoliated into single-layer flakes by micromechanical exfoliation [51, 52]. This method does not control flake thickness and size; however, and is
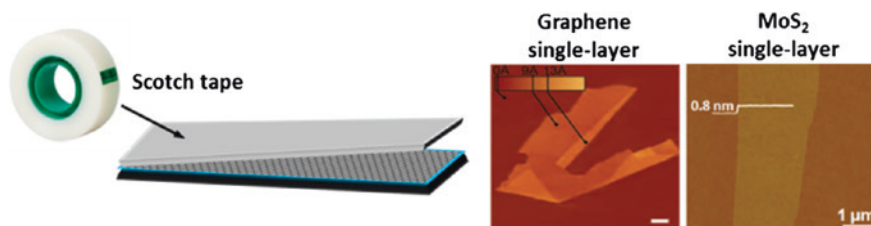
Fig. 3 Micromechanical exfoliation. AFM images of mechanically exfoliated single-layer graphene and MoS_2. (Reproduced with permission from: (graphene) Novoselov et al. 2005 [49]. Copyright © 2005 American Chemical Society). (MoS_2) (Reproduced with permission from Li et al. 2012 [50]. Copyright © 2012 John Wiley and Sons)

not appropriate for mass production, or for production of large $2D\text{-}MX_2$ single-layers. For energy harvesting/conversion and storage devices, 2D nanosheet-based devices require nanosheets of large surface area for solar cells, and large amounts of nanosheets for energy storage applications. Thus, this mechanical exfoliation method is used primarily for fundamental studies of new physics and new devices [32, 33, 40, 53–61].

2.2.2 Chemical Vapor Deposition

Among methods for graphene synthesis, CVD is widely used to produce uniform single-layer of large area [44, 62]. This is also the most appropriate method to synthesize $2D\text{-}MX_2$ single-layer with a vertically hybrid structure. This method also makes it possible to introduce dopants to $2D\text{-}MX_2$ to control bandgap [63].

A typical, low-pressure CVD system consists of a furnace with a quartz tube, for heat-vaporization of chalcogenides, and an outflux cold trap. The CVD synthesis of MoS_2 has involved precursors of various phases, such as MoO_3 and S powder vaporized and co-deposited onto substrate [64–66], sulfurization of pre-deposited Mo precursors (e.g., MoO_2 film [67, 68], MoO_3 film [68], Mo [35], aromatic molecules [69]), and decomposition of ammonium thiomolybdate ((NH_4)$_2MoS_4$) film under S gas [70].

Regarding the first case, CVD methods have been reported for creating MoS_2 single-layer on SiO_2/Si substrates by Lee et al. [64]. They reported that large-area MoS_2 sheets with 1–3 layers were directly synthesized on SiO_2/Si substrate by heating MoO_3 and S powder (Fig. 4). The synthesized MoS_2 showed high crystallinity in a six-fold hexagonal lattice and n-type semiconductor properties. Zhan et al. demonstrated that large-area MoS_2 could be synthesized by sulfurization of pre-deposited Mo film by e-beam evaporation [35]. The resulting film showed polycrystalline MoS_2 due to suppressed Mo migration because the melting point of Mo (2610 °C) was higher than the growth temperature (~750 °C). Another similar method was reported by Wang et al. [67]. They demonstrated formation of a MoS_2 bilayer 1.5 nm thick using layer-by-layer sulfurization of MoO_2
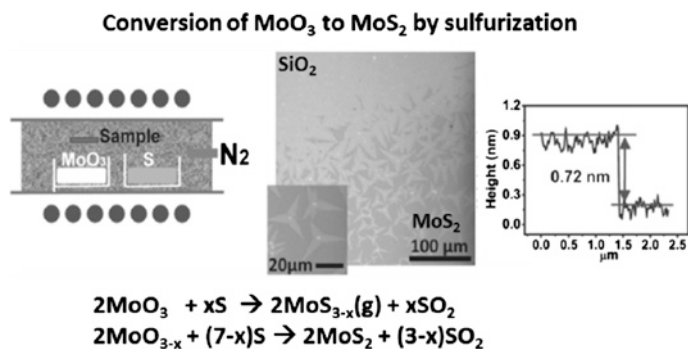
Conversion of MoO$_3$ to MoS$_2$ by sulfurization

$$2MoO_3 + xS \rightarrow 2MoS_{3-x}(g) + xSO_2$$
$$2MoO_{3-x} + (7-x)S \rightarrow 2MoS_2 + (3-x)SO_2$$

Fig. 4 Schematic illustration for CVD (*left*) and the optical image of MoS$_2$ on SiO$_2$/Si (*center*). The thickness of single-layer MoS$_2$ is 0.72 nm, which is measured by AFM (*right*). (Reproduced with permission from Lee et al. 2012 [64]. Copyright © 2012 John Wiley and Sons)

microplates at 850–950 °C. Using the weak adhesion between a MoS$_2$ layer and MoO$_2$ precursor film, MoS$_2$ flakes with domain size of 10 µm were obtained by separation from the MoS$_2$/MoO$_2$ film. MoS$_2$ synthesis using substrate dip-coated in (NH$_4$)$_2$MoS$_4$ solution and exposed to S gas was reported by Liu et al. [70]. These workers produced large-area MoS$_2$ film with uniform thickness in 2–3 layers. Sulfurization using pre-deposited metal precursor films is an effective method for preparation of large-area MX$_2$ single-layer.

Recently, Najmaei et al. reported forming triangular MoS$_2$ single-layer with large grain size and an edge-length of 10 µm using MoO$_3$ film on Si substrate [68] (Fig. 5a). Lee et al. demonstrated triangular MoS$_2$ sheets on various substrates using atmospheric pressure CVD (APCVD) with aromatic-molecule seeds (perylene-3,4,9,10-tetracarboxylic acid tetrapotassium salt, PTAS) [69] (Fig. 4b). In addition, there have been reports of demonstrations in which insulating single-crystals, such as sapphire, quartz, and mica, were used to form high quality 2D-MX$_2$ [71–76].

Formation of large-area MoS$_2$ single-layer was reported by van der Zande et al. [66]. They used solid MoO$_3$ and S precursors to produce large MoS$_2$ single-layer by APCVD growth. The resulting sheets of triangular MoS$_2$ had very long edge-length (~120 µm). Another large MoS$_2$ layer was grown on mica substrate, resulting in a continuous MoS$_2$ film of high uniformity, by coalescence of aligned MoS$_2$ domains [75].

Besides MoS$_2$, recently, our group reported CVD growth of large-area MoSe$_2$ single-layer with high quality and uniformity, on SiO$_2$/Si and sapphire substrate [73] (Fig. 6). A MoSe$_2$-graphene hetero-structure created by the CVD method was also demonstrated. It exhibited PL quenching by fast transfer of photogenerated charge carriers in the stacked heterostructure. Cong et al. reported triangular WS$_2$ single-layer with long edge-length (178 µm) formed in a modified quartz-tube furnace [77]. In this case, WO$_3$ and S powder were loaded into a small, inner quartz tube sealed on one side. By direct sulfurization of the WO$_3$, formation of
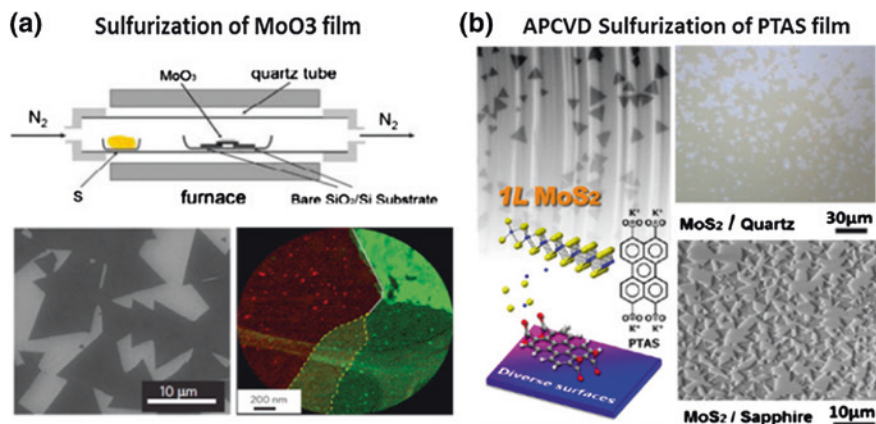
Fig. 5 **a** Schematic illustration for CVD (*upper*), SEM image (*bottom left*) and False-color dark-field TEM image of MoS$_2$ (*bottom right*) (Reproduced with permission from Najmaei et al. 2013 [68]. Copyright © 2013 Nature Publishing Group). **b** Chemical structure of PTAS (*bottom right*), schematic illustration of MoS$_2$ growth (*bottom left*) and SEM images of single-layer MoS$_2$ (*upper left*). Optical images of MoS$_2$ film on quartz (*upper right*) and sapphire (*bottom right*). (Reproduced with permission from Lee et al. 2013 [69]. Copyright © 2013 American Chemical Society)
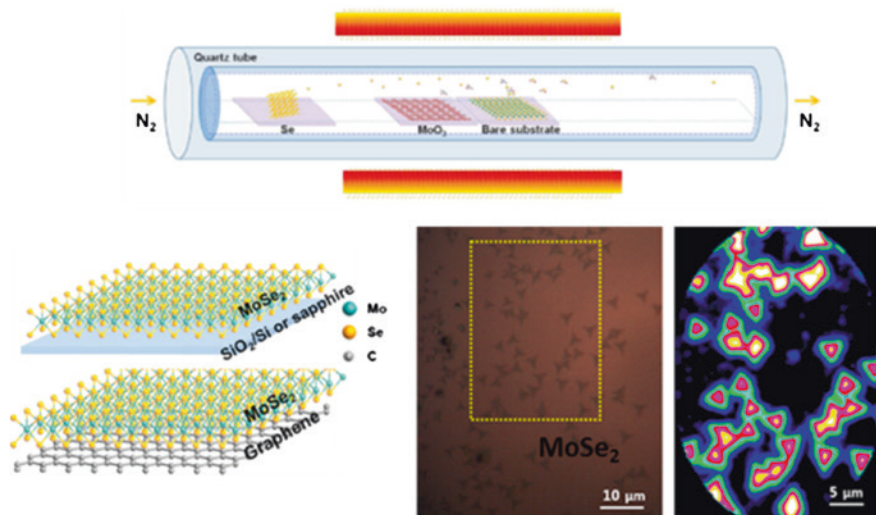

Fig. 6 Schematic illustration of CVD system (*upper*). The structure of MoSe$_2$ on SiO$_2$/Si (or sapphire) and graphene/SiO$_2$/Si substrate, respectively (*bottom left*). Optical image of MoSe$_2$ single-layer and PL intensity map for the yellow box shown in the left optical image (*bottom right*). (Reproduced with permission from Shim et al. 2014 [73]. Copyright © 2014 American Chemical Society)

large-area, WS_2 single-layer of high quality was demonstrated. First, triangular WS_2 sheets formed and then a few layer sheets grew at the apexes of the triangular sheets. Formation of large-area WSe_2 monolayer was also demonstrated using gas-phase reaction of WO_3 and Se powder in hydrogen [72].

The CVD method can produce MX_2 single-layer with large domain and high quality. In particular, well-aligned MX_2 domains may produce wafer-scale, single crystals by domain coalescence during CVD growth.

2.2.3 Liquid-Based Exfoliation

Graphene and $2D\text{-}MX_2$ can also be obtained by the liquid-based exfoliation method. This method is the most economic for mass production. Therefore, it has been considered a useful approach for obtaining large quantities of 2D nanosheets from bulk powder. Liquid-based exfoliation is a suitable method for applications that require large amounts, such as electrochemical energy storage, flexible energy devices, composite materials, inkjet printing, thin films, and spray coating.

Graphene Nanosheets

Liquid-based exfoliation involves sonication of graphite, intercalated graphite, or graphite oxide powder in suitable solvents [43, 78–80].

Graphite oxide Liquid-based exfoliation of graphite oxide is widely used for graphene production [41, 43, 81–89]. This method involves a two-step process: intercalation with strong oxidizing agents and expansion of graphite layers by sonication. These chemical processes introduce functional groups (i.e., epoxide, –OH, –COOH, and –COH groups) in the basal plane and at the edges [80] (Fig. 7). Thus, GO by oxidative exfoliation has a defective structure and insulating properties. The reduction of GO by thermal [89, 90], electrochemical [86, 88, 91], or chemical treatment [87, 90] can transform the insulating GO to conductive graphene, which is then referred to as reduced GO (rGO).

Direct exfoliation of graphite Direct liquid exfoliation of natural graphite can produce single- or few-layer graphene by ultrasonication in organic solvents (e.g., N-methyl-2-pyrrolidone (NMP), N,N-dimethylformamide (DMF), and benzyl benzoate) with suitable surface energy (40–50 mJ m^{-2}) [92]. This method gives the highest yield in NMP and high quality graphene with low defects. Although this type of exfoliation can be used directly to obtain conductive graphene sheets with low defects, this method has some disadvantages (e.g., very low yield, toxic solvents, and reaggregation).

Intercalated graphite Intercalated graphite formed by insertion of intercalant species between graphite layers can be used to expand the graphite-interlayer distance by rapid increase in the vapor pressure of inserted materials, during microwave or thermal treatment. This form of exfoliation provides a high-yield method
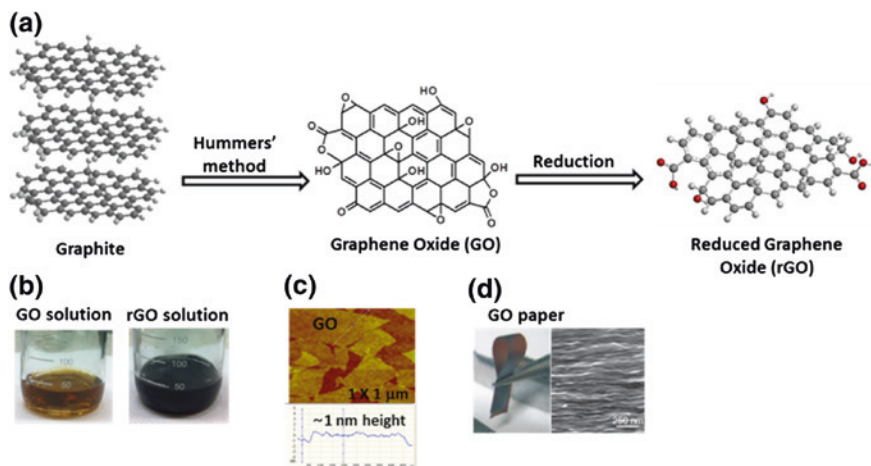
Fig. 7 **a** Scheme for GO synthesis and the structure of GO and rGO (*gray ball*: carbon, *red ball*: oxygen). **b** Optical image of GO and rGO solution, and **c** AFM image of GO sheets on SiO₂/Si with 1 nm height. **d** Optical image of GO paper (*left*) and SEM image (*right*) of cross-section of the GO paper. (Reproduced with permission from Dikin et al. 2007 [85]. Copyright © 2007 Nature Publishing Group)

of producing graphene with high quality and large lateral size. However, many methods for creating intercalated-graphite involve oxidation in ambient air and dangerous chemical reactions.

2D-TMD Nanosheets

With a layered structure similar to graphene, MX_2 can also be made to produce single-layer or few-layer MX_2 by liquid-based exfoliation. There are two pertinent types of liquid-based exfoliation: direct exfoliation by sonication in appropriate solvents and chemical exfoliation of Li-intercalated MX_2 in water.

Liquid-based direct exfoliation Direct exfoliation involves ultrasonication of bulk MX_2 powder in organic solvents and in aqueous surfactant solutions [93–97]. The efficiency of direct exfoliation depends on solvent, surfactant, and sonication time. Direct liquid exfoliation using organic solvents can produce single- or few-layer 2D-MX_2 through ultrasonication. Nanosheets of 2D-MX_2 also showed the highest yield in NMP as graphene. Coleman et al. demonstrated this form of direct exfoliation and reported surface energy of $65-75$ mJ m^{-2} for MoS_2, WS_2, and $MoSe_2$ [94, 96]. NMP has surface energy similar to MX_2. In the case of direct exfoliation using surfactants, the surfactants prevent the restacking of MX_2 nanosheets. However, these direct exfoliations exhibited very low yield ($2-10$ %), which also required lengthy sonication time to improve dispersion. Our group, has recently reported direct exfoliation of MoS_2 with alkali-metal-hydroxide
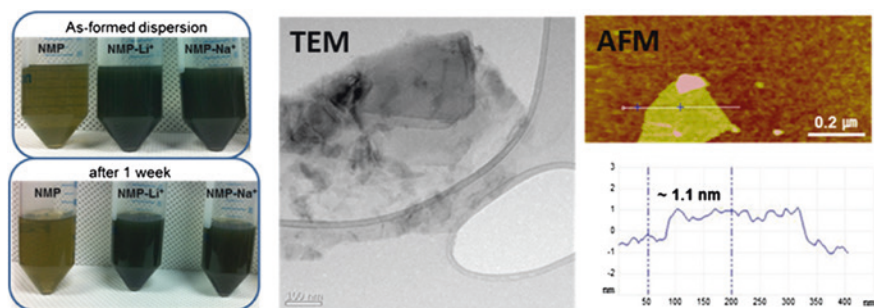
Fig. 8 Optical image of MoS$_2$ dispersion with alkali-metal assistant in DMF (*left*). TEM image and AFM image of the exfoliated MoS$_2$ single-layer. (Reproduced with permission from Bang et al. 2014 [93]. Copyright © 2014 American Chemical Society)
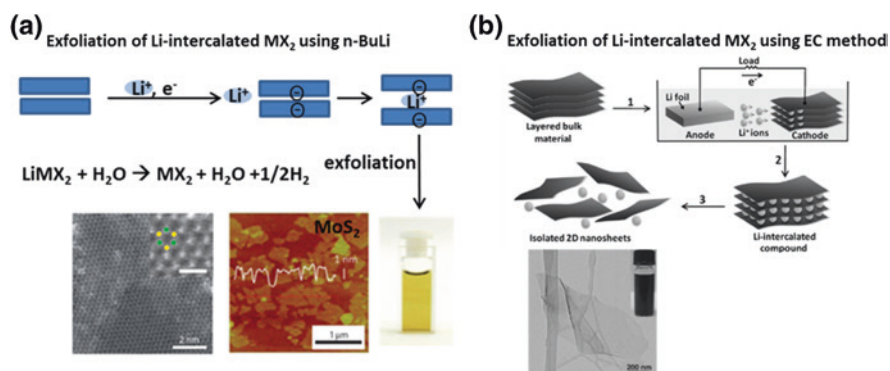

Fig. 9 **a** Schematic illustration for Li intercalation into MX$_2$ layers (*upper*) and optical image of the exfoliated MoS$_2$ dispersion in water. TEM image of MoS$_2$ single-layer and AFM image the exfoliated MoS$_2$ sheets (*bottom*). (Reproduced with permission from Eda et al. 2011 [26]. Copyright © 2011 American Chemical Society). **b** Schematic illustration for electrochemical lithiation (2) and exfoliation (3) of the Li-intercalated MX$_2$ (*upper*). TEM image of MoS$_2$ nanosheet. Inset: optical image of the exfoliated MoS$_2$ dispersion (*bottom*). (Reproduced with permission from Zeng et al. 2011 [98]. Copyright © 2011 John Wiley and Sons)

assistance to improve the direct-exfoliation efficiency [93] (Fig. 8). Our method exhibited high yield (65 %) and good dispersibility.

Liquid-based chemical exfoliation Liquid-based chemical exfoliation of Li-intercalated MX$_2$ in water gives a high yield of single-layer MX$_2$ (nearly 100 %). Bulk MX$_2$ is intercalated with Li using n-butyllithium (n-BuLi) [26] (Fig. 9a) or electrochemical lithiation [98, 99] (Fig. 9b), forming Li$_x$MX$_2$. Electrochemical lithiation can be controlled by adjusting the amount of Li ions inserted [99]. The Li$_x$MX$_2$ materials can easily be exfoliated using brief ultrasonication in water. The resulting 2D-MX$_2$ flakes showed single-layer thickness of 1–1.2 nm and metallic 1T phase. The initial 2H phase was induced to form the metallic 1T phase by

charge transfer from Li to MX_2. The induced 1T-phase can recover to the initial 2H phase upon annealing at temperatures of 200–300 °C [26]. This method is one of the most effective methods for mass production of metallic 2D-MX_2 single-layer.

3 Energy Harvesting and Energy Conversion Applications

3.1 Solar Cells

Solar energy is abundant and sustainable and has attracted interest for many years. Solar cells (dye-sensitized, polymer, organic, hetero-junction, and quantum-dot sensitized) are promising devices for conversion of solar energy into electricity. Graphene has been extensively investigated in relation to solar cell applications because of its high optical transparency, good mechanical flexibility, high thermal stability, and high electrical conductivity. For these reasons, it is now a candidate to replace indium tin oxide (ITO) in photovoltaics and opto-electronics. Graphene-analogs, such as 2D-MX_2 materials, have also potential as photovoltaic and opto-electronic materials. There have been reports of their use for transparent anodes or cathodes, catalytic counter electrodes, and the active layer for energy harvesting and conversion. In particular, heterostructures, such as those formed by combining 2D-MX_2 and graphene, have recently attracted attention as a new structure for light-harvesting applications. Heterostructures can induce significant photon absorption and photocurrent.

3.1.1 Graphene Nanosheets for Solar Cells

Graphene and graphene-based materials are attractive for solar energy harvesting and conversion. They have been investigated extensively for solar cell applications. As mentioned in Sect. 2.2, graphene has unique properties such as high carrier mobility, high optical transparency, very large surface area, high chemical and thermal stability, and high mechanical flexibility. It can be used in diverse ways as transparent anodes and cathodes, electron and hole-transport materials, catalytic counter electrodes, and active layers in solar cells.

Graphene as photo-anode In dye-sensitized solar cells (DSSCs), graphene can be used as photo-anode. Transparent indium tin oxide (ITO) and fluorine-doped tin oxide (FTO) are conventional electrodes used in DSSCs. However, indium is a rare-earth metal, mechanically brittle, and unstable under high temperature processing. Graphene, because of its high electrical conduction and optical transparency, may replace ITO in solar cells. Coleman et al. analyzed the transmittance and sheet resistance of graphene-based transparent electrodes from published data [100] (Fig. 10a). They mentioned that the conductivity of graphene could be increased by increasing the concentration of carriers. Bae et al. reported creation
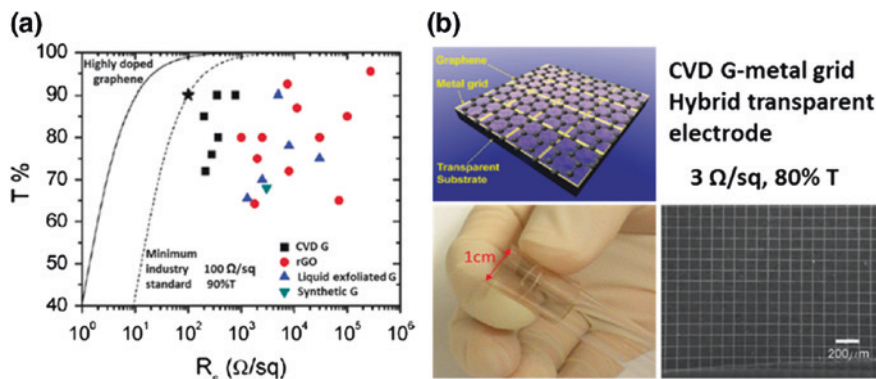
Fig. 10 **a** Plot for transmittance and sheet resistant from data in the published papers. (Reproduced with permission from De and Coleman 2010 [100]. Copyright © 2010 American Chemical Society). **b** Schematic illustration of hybrid film of CVD-graphene and metal grid as transparent electrode (*upper*). Optical image of the bendable transparent electrode (*bottom left*) and SEM image (*bottom right*) of CVD graphene-metal grid on PET. (Reproduced with permission from Zhu et al. 2011 [102]. Copyright © 2011 American Chemical Society)

of large-area CVD-graphene film (4-layered) with HNO_3 doping by the roll-to-roll method [101]. This acid-doped graphene film exhibited low sheet resistance (30 Ω/sq) with 90 % transmittance, which is superior to ITO electrodes. In addition to these, hybrid films of CVD-graphene and metal grid showed the best performance (3 Ω/sq with 80 % transmittance), in the form of bendable, transparent electrodes [102] (Fig. 10b).

Wang et al. reported rGO film used as a transparent conducting electrode in DSSCs [103]. The rGO film exhibited conductivity of 550 S cm^{-1} with 70 % transmittance (1000–3000 nm). However, DSSCs using rGO film (device structure: rGO/TiO_2/dye/spiro-OMeTAD/Au) showed very low power-conversion efficiency (PCE) of 0.26 %. Li et al. reported the use of GO film as the hole-transport layer in organic solar cells (OSCs) [104]. The OSC using GO film (device structure: ITO/GO(2 nm)/P3HT:PCBM/Al) had PCE of 3.5 ± 0.3 %. DeArco et al. reported flexible CVD-graphene films on polyethylene terephthalate (PET) film [105]. The CVD-graphene on transparent PET film showed sheet resistance of 230 Ω/sq with 72 % transparency. Organic solar cells using this CVD-graphene as flexible transparent anode exhibited 1.27 % PCE and good performance under bending of up to 138° (Fig. 11). For use in high performance organic solar cells, Hsu et al. reported a CVD graphene-tetracyanoquinodimethane (TCNQ) multi-layer anode with the resistance of 182 Ω/sq and 88 % transmittance [106]. The OSC using graphene-TCNQ (device structure: Graphene-TCNQ/PEDOT:PSS/P3HT:PCBM/Ca/Al) showed 2.58 % PCE.

CVD-graphene and rGO can be used as diverse roles in solar cells. CVD-graphene is more attractive as transparent conducting electrode due to their high electrical conductivity and relative inertness compared to rGO.
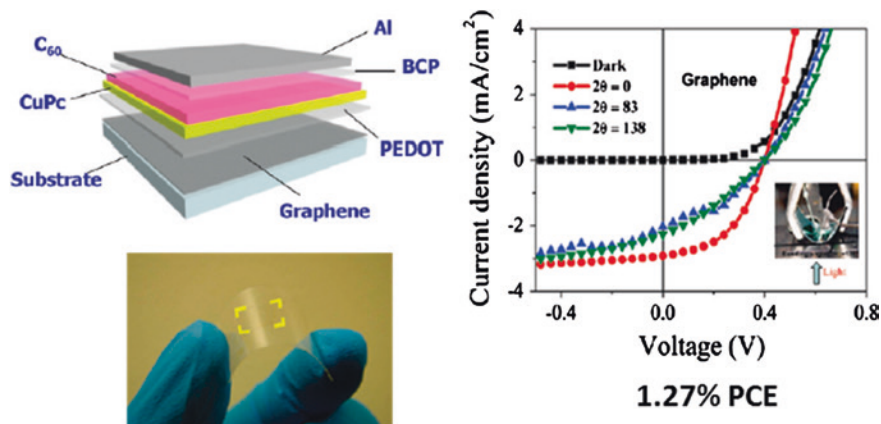
Fig. 11 Schematic illustration of the organic solar cell with CVD graphene as anodic electrode (*upper*). Current-voltage characteristic curves for the photovoltaic device under A.M. 1.5 illumination at 100 mW cm^{-2} for different bending angles (*bottom*). (Reproduced with permission from De Arco et al. 2010 [105]. Copyright © 2010 American Chemical Society)

Graphene as catalytic counter electrodes Graphene is also a promising material for use as catalytic counter electrodes (CE) in DSSCs due to its low cost, high surface area, high conductivity, and electrocatalytic properties. Many works have reported using graphene and graphene composites as catalytic CEs in Pt-free DSSCs. Recently, Gong et al. demonstrated that rGO embedded in a polypyrrol (ppy) matrix, is a good candidate conductive and catalytic CE in DSSCs [107]. Certain DSSCs (device structure FTO/TiO$_2$/dye/I$_3$, I$^-$ mediated electrolyte/rGO-ppy) exhibited a high PCE of 8.14 %, which is comparable to a Pt counter electrode (8.34 % PCE). This rGO-ppy electrode can be considered a promising CE for Pt-free DSSCs.

Graphene Quantum Dots (GQDs) GQDs are graphene nanoparticles with lateral size less than 100 nm. They have excellent properties that include high optical absorptivity [108–110]. Yan et al. first reported GQD-sensitized DSSC [111]. Zhang et al. demonstrated that graphene synthesized by a hydrothermal method could act as a photosensitizer [112]. Recently, Williams et al. suggested that photoexcited GQDs inject electrons into TiO$_2$ within 15 fs [113].

Metallic graphene with a semiconductor can form Schottky-junction layer in DSSCs. Miao et al. reported an enhanced Schottky-junction solar cell formed using chemical-doped graphene/n-Si [114]. The graphene had been doped with bis(trifluoromethanesulfonyl)-amide (TFSA). The TFSA-doped graphene showed low sheet resistance and increased work function. This solar cell exhibited a high PCE (8.6 %). Song et al. reported the rGO-TiO$_2$ Schottky-junction in a DSSC (device structure: FTO/graphene-TiO$_2$/dye/I$_3$, I$^-$ mediated electrolyte/Pt). DSSC using rGO-TiO$_2$ showed an improved PCE (6.06 %) compared to pure TiO$_2$ without rGO [115]. Liu et al. reported GO (work function of 4.6–4.8 eV) used for hole

transport and Cs-doped GO (work function of 3.9–4.1 eV) for electron transport in polymer solar cells [116].

Thus, graphene and graphene derivatives could be widely used to improve the performance of solar cells. These materials have high electrical conductivity and optical transparency, and are promising candidates to replace ITO in solar cells.

3.1.2 Nanosheets of 2D-TMDs for Solar Cells

Nanosheets of 2D-MX_2 have recently been receiving a lot of interest due to their role as semiconductors with a small direct bandgap (1–2 eV) and n or p-type carriers depending on their layer thickness and elemental compositions [22]. They can absorb significant portions of the solar spectrum, and may be considered efficient nanomaterials for use in solar energy conversion. These 2D-MX_2 sheets have higher sunlight absorption (5–10 % in visible range at 6.5 Å thickness) than the commonly used absorbers, Si and GaAs [117]. Moreover, the 2D-MX_2 single-layer is flexible, transparent, and ultrathin. Thus, 2D-MX_2 single-layer can be used as an efficient photovoltaic material.

2D-TMDs for cathode catalysts In DSSC, platinum (Pt) is widely used as a cathode material due to its excellent electrocatalytic properties. However, it has several disadvantages in DSSC applications (i.e., high price and limited reserves). To replace expensive Pt electrodes, 2D-MX_2-based materials have been studied for use as cathode catalysts in DSSC. When DSSC was chemically synthesized using MoS_2 and WS_2 it exhibited power conversion efficiency (PCE) of 7.59 and 7.73 %, respectively [118]. Recently, Patil et al. prepared MoS_2 from $MoCl_5$ and thioacetamide at low temperature (70 °C) and under wet conditions [119]. This DSSC exhibited 7.01 % PCE, which is comparable to DSSC with a Pt counter electrode (7.31 %). Chen et al. reported the few-layer $MoSe_2$ fabricated by surface selenization of Mo-coated glass in a CVD system [120]. The few-layer $MoSe_2$ DSSC showed a higher PEC (9 %) than a counter electrode based on Pt nanoparticles on FTO glass. MoS_2 and graphene composite as a counter electrode in DSSC showed a PEC of about 6 % [121, 122]. The 2D-MX_2-based CE exhibited good performance, and are very useful for replacement of Pt in DSSCs.

2D-TMDs for polymer solar cells 2D-MX_2-based materials have been studied for applications in polymer solar cells. Yu et al. reported a MoS_2-Au Schottky-junction solar cell with 1.8 % PCE [123]. In the same group, a MoS_2-TiO_2 composite structure with a P3HT active layer (device structure: ITO/TiO_2/MoS_2/P3HT/Au) exhibited 1.3 % PCE under 100 mW cm^{-2} illumination [124]. Recently, Yun et al. reported creation of a polymer solar cell using p- and n-doped MoS_2 film for modulation of the work function of the interfacial layer. A P-doped MoS_2 hole-transport layer showed enhanced performance (3.4 % PCE) in a polymer solar cell [125]. Gu et al. prepared a 2D-MoS_2 single-layer (AFM image in Fig. 13) using liquid-based exfoliation from Li-intercalated MoS_2 [126]. A device using liquid-exfoliated 2D-MoS_2 nanosheets as a hole-extraction layer exhibited 4.03 % PCE for the P3HT:$PC_{61}BM$ active layer and 8.11 % PCE for
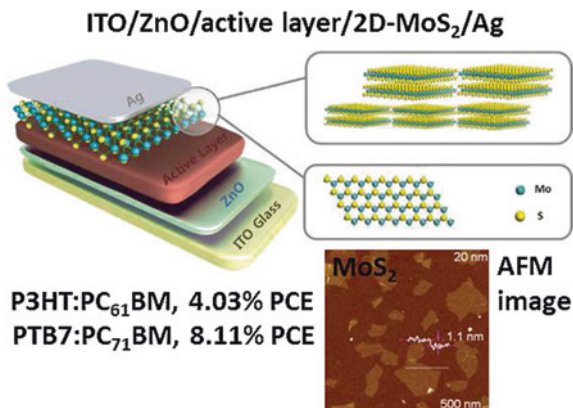
the PTB7:PC_{71}BM active layer, respectively (Fig. 12). Niu et al. reported single and few-layer 2D-TMDs nanosheets obtained by salt-assisted liquid exfoliation [127]. Some OSCs using the 2D-MoS_2 nanosheets as hole-transport layers and P3HT:PC_{61}BM as the photoactive layer (device structure: ITO/2D-MoS_2/ P3HT:PC_{61}BM/Al) showed 1.81 % PCE under AM 1.5 illumination. Recent OSCs using MoO_3/MoS_2 exhibited a PCE of 6.9 % and high air-stability of 5.5 % PCE after 16 days [128]. These results also demonstrate that 2D-MoS_2-based nanosheets are a promising hole-transport material for high performance solar cells. To improve light harvesting in OSCs, plasmonic OSCs using MoS_2-Au NP composite (MoS_2@Au) as the hole-transport layer exhibited enhanced short-circuit photocurrent density, and a PCE of 7.25 % [129].

Heterostructure of 2D-TMDs Van der Waals heterostructures of semiconducting MX_2 have recently attracted attention as a new structure for light-harvesting applications [117, 130–135]. Britnell et al. prepared vertical heterostructures of MX_2-graphene using 2D-MX_2 as good photoactive materials and graphene as a good transparent electrode [135]. They demonstrated effective photovoltaic devices with photosensitivity above 0.1 A W^{-1} using vertical MX_2-graphene heterostructures. From DFT calculation, Bernardi et al. predicted the performance of heterojunction solar cells with a Schottky barrier (MoS_2-graphene) and bilayer excitonic MX_2 (MoS_2-WS_2) [117]. They estimated 0.4–1.5 % PCE for a bilayer of MoS_2-WS_2 1.2 nm thick, and 0.1–1.0 % PCE for a bilayer of MoS_2-graphene 0.9 nm thick. Recently, Lopez-Sanchez et al. reported a diode based on a p–n heterojunction of single-layer MoS_2 and p-type silicon [132]. This heterojunction diode of MoS_2-Si operates as a photovoltaic device, which converts incident light into electrical power with an external quantum efficiency (EQE) of 4.4 %. Lee et al. fabricated at sandwiched p–n heterojunction of n-MoS_2 and p-WSe_2 single-layer between graphene layers, and measured the external quantum efficiency [134] (Fig. 13). The reported EQE of the p-WSe_2/n-MoS_2 heterojunctions of different thicknesses were 2.4, 12, and 34 % for single layer, bilayer, and multilayer, respectively. In addition, Hong et al. reported the experimental observation of ultrafast hole-transfer within 50 fs in the stacked heterostructure of MoS_2
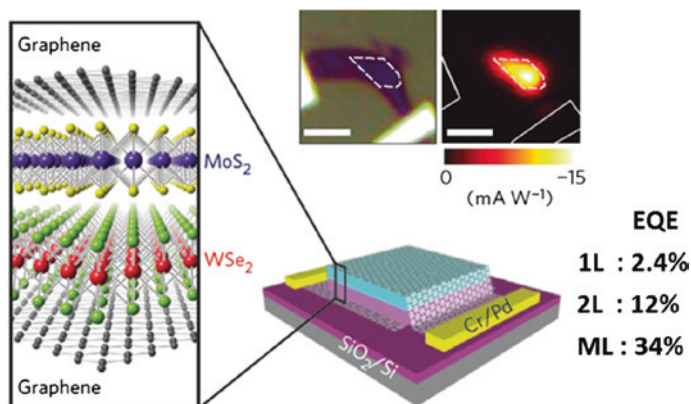
Fig. 13 Schematic illustration of Graphene/n-MoS$_2$/p-WSe$_2$/Graphene. (Reproduced with permission from Lee et al. 2014 [134]. Copyright © 2014 Nature Publishing Group)

and WS$_2$ [133]. Heterostructures of semiconducting 2D-MX$_2$ can enhance light–matter interaction, which induces major photon absorption and production of photocurrent.

Semiconductors of 2D-MX$_2$ are materials that separate electrons and holes for energy conversion. The physical properties of heterostructures using them can be controlled to induce fast charge-separation. Therefore, 2D MX$_2$-based devices are promising for light-harvesting and conversion.

3.2 Fuel Cells

Fuel cells are clean, sustainable energy conversion devices that convert chemical energy of a fuel directly into electricity. These technologies are approaching commercialization in small portable power sources [136]. The key parts of a fuel cell are electrodes for fuel oxidation (anode) and oxygen reduction (cathode) (Fig. 14). Expensive noble metals are well-known active catalysts for both anodes and

Fig. 14 The structure of fuel cell
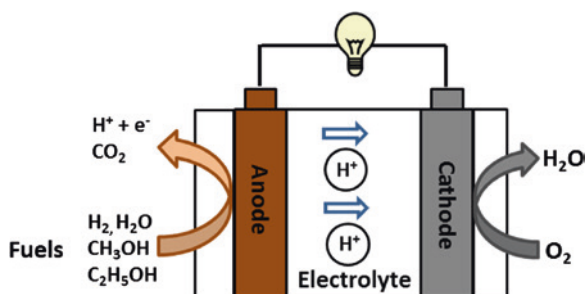
cathodes in fuel cells. Among them, platinum-nanoparticles are regarded as the best catalyst, and they have the highest electrocatalytic activity for oxygen reduction at the cathode. However, Pt has several disadvantages in practical applications of fuel cells. These include its high price, limited (global) reserves, and deactivation by self-poisoning from CO adsorption. Therefore, it is essential to develop low-cost non-platinum catalysts. The activities of catalysts depend on their surface properties. Good catalysts for high performance and commercialization require low cost, high surface area, maximum contact area, good electronic conductivity, and high electrochemical stability in acidic and alkaline electrolytes. Graphene has received a great deal of attention as a good catalyst due to its high surface area, good chemical and environmental stability, and unique structures. Graphene-analogous 2D-MX_2 has also begun receiving considerable interest recently.

3.2.1 Graphene Nanosheets for Fuel Cells

Oxygen reduction reaction (ORR) at the cathode The oxygen reduction reaction determines the overall performance of a fuel cell. Pt nanoparticles are the best catalysts and are still used in practical applications due to their high catalytic activity and good stability. Graphene-based Pt nanoparticles have been also studied for ORR [13, 137–142]. However, Pt has the disadvantage of reserves that are too limited, and prices that are too high for the commercialization of fuel cells. Therefore, development of Pt-free catalysts is important for commercialization of fuel cells. Many researchers have addressed the electrocatalytic activity of metal-free graphene-based nanomaterials. These graphene-based nanomaterials exhibited enhanced catalytic activity and durability when used for ORR in fuel cells. Graphene appears to be a promising candidate as catalyst support than commercial Pt-C due to high surface area, high electrical conductivity, 2D nanosheets with atomic layer, basal-plane structure of sp^2-hybridized carbon, and good stability [13, 140–149].

As metal-free alternatives, metal-free graphene-based nanomaterials are important for commercialization of fuel cells. As a result, metal-free graphene-based nanomaterials have been extensively developed for ORR [13, 140–142, 150–161]. Heteroatom-doped graphene is one of the metal-free nanocatalysts. Heteroatom doping can induce charge redistribution in graphene and create active sites for oxygen adsorption. Heteroatom-doped graphene induces intramolecular charge transfer between graphene and dopants, and exhibits high catalytic activity and stability. Qu et al. reported creating N-doped graphene by growth of CVD graphene with ammonia [140]. The resulting N-doped graphene has shown higher catalytic activity and stability than commercial Pt/C. Yang et al. reported an S-doped rGO with good catalytic activity [141]. Li et al. synthesized N-doped graphene quantum dots (N-GQDs) with oxygen rich functional groups [142]. Zhang et al. reported amine-functionalized rGO with good performance for ORR [13]. These heteroatom-doped graphenes provided advantages as ORR catalysts. Although it is still not exactly clear about the active sites, theoretical and

experimental studies suggest that heteroatom-based graphene or its composites may provide metal-free catalysts with high activity and low cost.

Fuel oxidation at the anode Graphene-based noble metals have been attractive as anode material for use in direct methanol fuel cells (DMFCs). Methanol is a fuel appropriate for fuel cells, and the methanol oxidation process includes methanol adsorption and subsequent dissociation into adsorbed intermediates [162]. As mentioned earlier, CO-poisoning can greatly reduce the catalytic activity of Pt NPs [163]. In the case of the rGO-Pt NP catalysts, the oxygen-containing functional group of rGO or graphene can improve the electrocatalytic activity by removing the adsorbed CO from Pt sites [164]. Actually, the rGO-Pt nanoparticles exhibited higher catalytic performance than commercial Pt/C catalyst for the methanol oxidation reaction [143–148, 163–165]. Li et al. reported high catalytic activity for methanol oxidation using rGO-Pt nanoparticle (rGO-PtNPs) electrodes [145]. The graphene-based alloy metal NPs (e.g., PtRu-graphene, PtNi-graphene, and PtPd-rGO, PtFe-graphene) also displayed high electrocatalytic activities for methanol oxidation. Zhao et al. used one metal-free graphene-based nanomaterial (rGO-PPy-PdNPs) as anode [164]. In addition to methanol, the catalytic activity of graphene-based metal NPs catalysts has also been studied for use in oxidation reaction of ethanol [166, 167], formic acid [167–169], and hydrogen [163].

Graphene-based nanomaterials can be used as catalyst at both anodes and cathodes in fuel cells. Further study is necessary to determine the exact catalytic mechanisms needed to develop graphene-based catalysts with high activity and durability.

3.2.2 Nanosheets of 2D-TMDs for Fuel Cells

Hydrogen is a clean fuel that leaves only water behind when used, and is one of the promising new energy sources. To produce hydrogen in a fuel cell effectively, an electrocatalyst is required. As already known, Pt is the best known electrocatalyst for the hydrogen evolution reaction (HER), though it has the disadvantages mentioned previously. Layered MX_2 products are made from abundant materials, and 2D-MX_2 nanosheets have received increasing attention as HER catalysts for fuel cells [170–172].

2D-TMDs for HER catalysts As seen in Sect. 2.1.2 (CVD), 2D-MX_2 nanosheets exhibit the shape of triangle or truncated triangles. Their structure has two different edge sites: X and M [173] (Fig. 15a). The elements Co and Ni incorporated into MoS_2 induce morphology change resulting in truncated triangles with prominently exposed S edge [174]. The ratio of the length of the basal plane to that of the edge sites changes with the size of the nanosheet. These edge sites are related to HER activity. In density-functional calculations, the free energy for hydrogen adsorption on the MoS_2 edge was shown to be similar to the activity of biological catalysts [170] (Fig. 15b).

Jaramillo et al. [172] experimentally demonstrated that MoS_2 edges are catalytically active sites for HER. Since then, Kibsgaard et al. synthesized double-gyroid
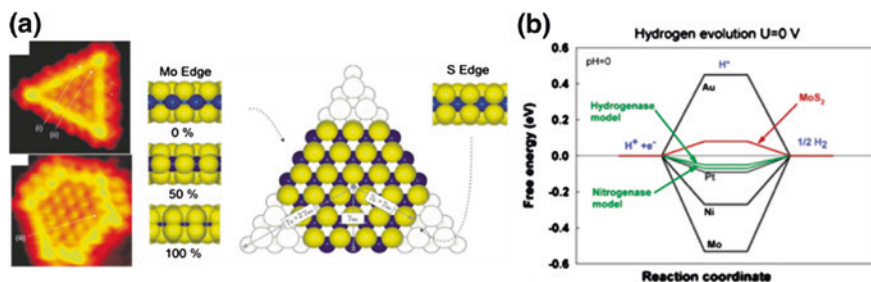
Fig. 15 **a** STM images of MoS_2 single-layer (*left*) and white lines for the scan orientation. *Top view* of atomic ball model of the truncated MoS_2 (*right*, Mo atoms: *blue*, S atoms: *yellow*). (Reproduced with permission from Lauritsen et al. [173]. Copyright © 2004 Elsevier). **b** Free energy diagram for hydrogen evolution by density functional calculations. (Reproduced with permission from Hinnemann et al. 2005 [170]. Copyright © 2005 American Chemical Society)
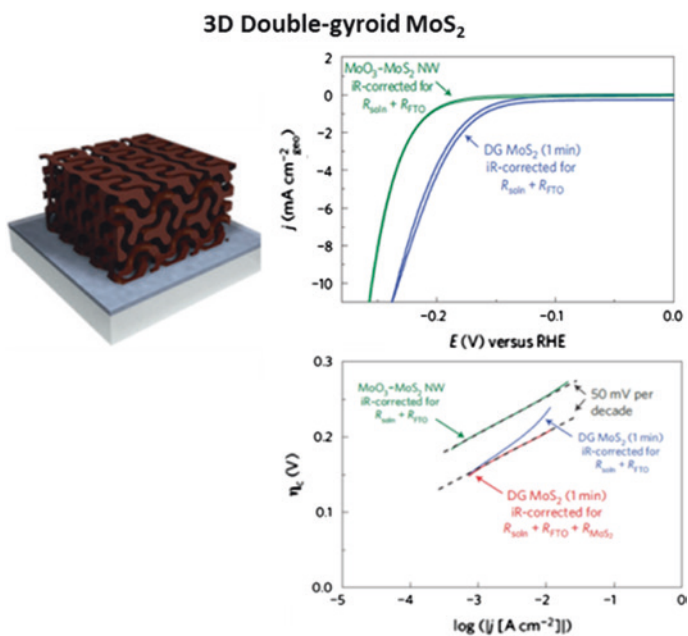
Fig. 16 The mesoporous structure of double-gyroid MoS_2 (*left*). CVs of the double-gyroid MoS_2 electrode at 5 mV s^{-1} (*right upper*) and tafel plot (*right bottom*). (Reproduced with permission from Kibsgaard et al. 2012 [171]. Copyright © 2012 Nature Publishing Group)

MoS_2 to largely expose the edge sites [171] (Fig. 16). This double-gyroid MoS_2 exhibited high activity, with a Tafel slope of 50 mV decade^{-1}. An amorphous MoS_2 with many defects also exhibited catalytically activity, with an average Tafel slope of 50 mV decade^{-1} [175–177].

As mentioned in Sect. 2.1 (Electronic structure), the symmetry of single-layer 2D-MX_2 has trigonal prismatic (2H phase) or octahedral (1T phase) coordination for transition-metal atoms [22]. Materials of 2D-MX_2 with 2H phase are mainly semiconducting, whereas 1T phase is metallic. Moreover, 2D-MX_2 nanosheets chemically exfoliated with Li intercalation exhibit metallic properties after phase change from 2H to 1T. An MX_2 single-layer in 1T phase was much more active for HER than in 2H phase [99, 178, 179]. The higher activity can be attributed to the presence of the metallic 1T phase. In particular, strained single-layer 1T-WS_2 produced by chemical exfoliation with Li intercalation exhibited excellent catalytic activity for HER [179]. Yi et al. demonstrated the correlation between MoS_2 properties and HER activity by electrochemical tuning of Li intercalation [99]. They also reported that 1T-MoS_2 have high catalytic activity for HER. In other work, MX_2-graphene hybrid types were used as catalysts for HER [180, 181]. Li et al. reported use of a MoS_2-rGO hybrid to improve the conducting network and edge sites, and this hybrid exhibited excellent electrocatalytic activity with high current, low over-potential of -0.1 V and a low Tafel slope of 41 mV decade^{-1} [181]. Liao et al. synthesized MoS_2 NPs on mesoporous graphene sheet (MoS_2 NPs-MGF) with high surface area and conductive skeleton, and this product showed high electro-catalytic activity with rapid electron transfer and a low Tafel slope of 42 mV decade^{-1} [180]. A WS_2-rGO hybrid exhibited electrocatalytic activity with a Tafel slope of 58 mV decade^{-1}. There are also studies in which noble-metal NPs (Pt and Au)-MoS_2 nanosheets [182, 183] were used for HER and Pd-MoS_2 [184] for methanol oxidation. The hybrid materials showed higher HER activity than pure 2D-MoS_2 or WS_2. High HER performance was shown using 2D-MX_2 or 2D MX_2-G hybrid types (amorphous sheets, defective nanosheets, porous structure, and metallic 1T phase) with highly active sites. A summary of MX_2-based HER catalysts is provided in Table 2.

Table 2 MX_2-based HER catalysts

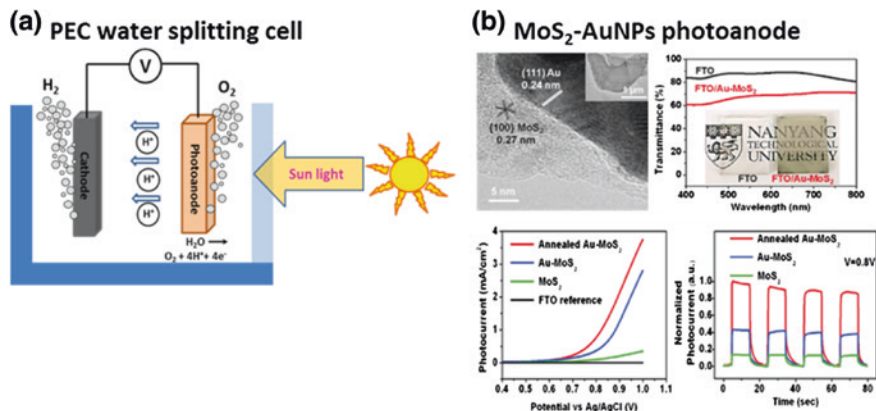| Material	Tafel slope (mV/decade)	References
MoS_2 nanoparticles	55–60	[172]
Double-gyroid MoS_2	50	[171]
Amorphous MoS_2	40	[177]
Defect-rich MoS_2	50	[176]
1T-MoS_2 nanosheets	40–44	[99, 185, 186]
1T-WS_2 nanosheets	60	[179]
MoS_2-rGO	41	[181]
MoS_2 on MGF	42.8	[180]
WS_2-rGO	58	[187]
Pt on single-layer MoS_2	40	[183]
Pt-2H MoS_2	110	[185]
Pt-1T MoS_2	43	

Fig. 17 **a** The structure of PEC water splitting cell. **b** TEM image of Au NPs on MoS$_2$ (*upper left*) and transmittance versus wavelength for MoS$_2$-Au NPs on FTO (*upper right*). LSVs for PEC with MoS$_2$-Au NPs photoanode in 0.1 M KH$_2$PO$_4$ under visible light of 350 mW cm^{-2} (*bottom left*) and normalized amperometric I-t cycles at 0.8 V for PEC on MoS$_2$-Au NPs photoanode (*bottom right*). (Reproduced with permission from Yin et al. 2014 [188]. Copyright © 2014 John Wiley and Sons)

2D-TMDs for water-splitting catalysts Semiconductor-based photocatalysts can be used for hydrogen production from photoelectrochemical (PEC) water splitting powered by solar energy (Fig. 17a). Single-layer 1H-MoS$_2$ is a photoactive semiconductor with a direct bandgap of 1.8 eV, which exhibits quantum confinement and excellent catalytic activity. Bandgaps of the 2D MX$_2$ single-layer can be matched with the visible region of the solar spectrum (1−2 eV). Therefore, the 2D MX$_2$ single-layer can absorb more sunlight, which can lead to high efficiency. Very recently, the Au-MoS$_2$ composite photo-anode exhibited enhanced photocatalytic water splitting under visible light [188] (Fig. 17b).

To achieve high efficiency of solar energy conversion, the development of active semiconductors under visible-or-longer wavelength regions will become important. Nano materials of 2D MX$_2$ are potential candidates for renewable hydrogen production. However, many challenges remain regarding solar hydrogen fuel.

4 Energy Storage Applications

Batteries and supercapacitors are important electrochemical energy storage devices, and have been extensively developed for a wide range of applications. The use of these energy storage devices in many energy-related products demands high energy storage capability, power delivery capability, and cycle stability. The rapid advance of these technologies depends on the development of better electrode materials. Nanostructured materials offer excellent energy storage, long life-cycles, and high rate capability.

Atomically thin graphene and 2D-MX_2 nanosheets have also attracted attention for use as electrode materials and electrode assistants for developing energy storage devices.

4.1 Lithium-Ion Batteries

Li-ion batteries (LIBs) have the significant advantages of low weight and higher energy storage. They are at the heart of the most promising energy storage systems for portable electronic devices and future electric vehicles. An LIB system consists of three parts: anode, cathode, and electrolyte. Commercial batteries utilize graphite as anode and lithium cobalt oxide ($LiCoO_2$) as cathode. The electrode materials are closely related to battery performance. Fast insertion and extraction of Li ions can be sustained using 2D nanosheets of materials such as graphene and MX_2. They are ultrathin, flexible, stretchable, and have high surface area, which will be useful for development of future portable, flexible devices.

4.1.1 Graphene Nanosheets for LIBs

Graphite is a common anode-electrode material in LIBs, but exhibits low Li storage capacity. The theoretical capacity of graphite is 372 mAh g^{-1} for LiC_6 [189]. Great efforts have been great made to overcome the capacity limitations of graphite for use in advanced LIBs. Graphene has received significant interest as an electrode material due to its high specific surface area, good chemical and thermal stability, wide potential window, high electrical conductivity, and excellent mechanical flexibility. The theoretical surface area of graphene is 2630 m^2 g^{-1} [7]. This is much higher than that of graphite (~ 10 m^2 g^{-1}) and CNT (~400 m^2 g^{-1}). Thus, atomically thin graphene can be considered an electrode material with good power capability for electrochemical energy storage. In particular, chemically prepared rGO offers a large number of porous sites, good conductivity, and increased interlayer spacing. Furthermore, they can be made to form layered structures with large interlayer space. The specific capacity of rGO sheets, with specific surface area of 492.5 m^2 g^{-1}, was 1264 mAh g^{-1} at 100 mA g^{-1}, a value higher than that of graphite [190]. However, the rGO electrode showed limited rate capability with capacity fluctuation due to induction of instability during lithiation and de-lithiation. To improve the rate capability, N or B-doped graphene has been used. It showed high rate capability and high specific capacity (1043 mAh g^{-1} for N-doped graphene and 1540 mAh g^{-1} for B-doped graphene) [19]. The high performance of these doped-graphene electrodes is due to fast Li-ion diffusion and electron transport supported by heteroatomic defects, increased interlayer distance between graphene sheets, improved electrical conductivity, and thermal stability. Graphene sponges could increase porosity, resulting in improved capacity. However, porosity also reduces the volumetric capacity and leads to a

large amount of electrolyte insertion, resulting in increased irreversible capacity. The first-cycle capacity of rGO sponge was 1059 mAh g^{-1} at 50 mA g^{-1}, but the capacity after a few cycles was only 400 mAh g^{-1} at 50 mA g^{-1} [191]. In the first cycle, mesoporous graphene had a specific capacity of 3535 mAh g^{-1} at 100 mA g^{-1}, but only 1040 mAh g^{-1} in the second cycle [192]. Graphene itself used as electrode material show low rate capability, poor cycle stability, and much lower capacity than a silicon-based anode (4200 mAh g^{-1}).

For high performance LIBs, graphene-based hybrid composites have been widely explored as electrode materials. These include graphene-metal oxide composites, graphene-2D MX_2 composites, graphene-CNT composites, and graphene-Si nanoparticle composites. In graphene-based composites, graphene can act as a highly conductive layer and as a mechanical support layer. The hybrid composites may reduce restacking of graphene layers and maintain a highly active surface area. Thus, Li storage capacity and the cycling performance of graphene-based hybrid composites can be enhanced. For example, the specific capacity of rGO-Fe_2O_3 composite in the 1st and 50th cycles exhibited 1693 and 1027 mAh g^{-1} at 100 mA g^{-1}, respectively [193]. Honeycomb film of 3D rGO-dimethyldioctadecylammonium (rGO-DODA) showed a large specific capacity of about 3025 mAh g^{-1} in the first cycle and a reversible capacity of 1612 mAh g^{-1} at 50 mA g^{-1} [194]. A graphene-silicon hybrid structure may significantly improve the energy density. The rGO-Si nanoparticle composite (SiNP@rGO) exhibited specific capacity of 2920 mAh g^{-1} in the first cycle and capacity of over 1205 mAh g^{-1} after 150 cycles with high cycling stability [195]. Sandwiching Si nanowires in rGO creates 3D porous structure (SiNW@G@rGO) produced a reversible capacity of 1600 mAh g^{-1} at 2100 mA g^{-1} [196]. Porous 3D graphene networks connected with Sn nanoparticles encapsulated within graphene shells (Sn@G-PGNW)were used as LIB anode [9]. Its capacity was 1022 mAh g^{-1} at 0.2 C and it exhibited very long-term cycle stability with capacity of 96.3 % after 1000 cycles. Graphene-based hybrid structures have shown better performance than bare graphene. Generally, graphene-Si composites showed high capacity (more than 2000 mAh g^{-1}). Various graphene-based anode materials useful for LIBs have been listed in Table 3.

One-atom-thick graphene was also studied for use in flexible LIBs, due to its high surface area, excellent flexibility, high conductivity, and short ion diffusion length. Graphene paper is highly conductive and mechanically strong with a Young's modulus of 41.8 GPa and a tensile strength of 293.3 MPa [197]. Some groups have demonstrated it using conductive rGO paper or CVD graphene. This graphene paper exhibited a capacity of 822 mAh g^{-1} at 50 mA g^{-1} [198]. The battery using CVD graphene can be bent and showed energy density of 10 Wh L^{-1} at 50 W L^{-1} with good cycle stability over 100 cycles [12]. These flexible batteries using graphene have shown good flexibility, high capacity, high rate, and long cycle performance even under conditions of repeated bending.

Graphene also serves as cathode material due to its high capacity and long cycle stability. $LiFePO_4$-CVD graphene sponge as cathode material exhibited a reversible capacity of 120 mAh g^{-1} at 10 °C without capacity loss after 500 cycles [199]. Composite sponge of rGO-VO_2 ribbons 10 nm thick showed a high reversible

Table 3 Graphene-based anode materials for LIBs

Material	Surface area $(m^2\,g^{-1})$	Capacity $(mAh\,g^{-1})$	Cycle stability $(mAh\,g^{-1})$	References
rGO	492.5	1264 at 0.1 A/g	848 after 40 cycles	[190]
N-doped rGO	290	1043 at 0.05 A/g	872 after 30 cycles	[19]
B-doped rGO	256	1549 at 0.05 A/g	1227 after 30 cycles	[19]
rGO sponge		1059 at 0.05 A/g	82 % capacity retention after 100 cycles	[191]
Mesoporous graphene	281	3535 at 0.1 A/g	1040 at the 2nd cycle	[192]
			833 after 60 cycles	
rGO-Fe$_2$O$_3$		1693 at 0.1 A/g	1027 after 50 cycles	[193]
rGO-DODA honey-comb film		3025 at 0.05 A/g	1612: reversible capacity, 1150 after 50 cycles	[194]
SiNP@rGO		2920 at 0.1 A/g	1720: reversible capacity, 1205 after 150 cycles	[195]
SiNP@G@rGO		1600 at 2.1 A/g	80 % capacity retention after 100 cycles	[196]
Sn@G-PGNW		1022 at 0.2 C	96.3 % capacity retention after 1000 cycles	[9]

specific capacity of 415 mAh g^{-1} at 1 C and cycle stability of 10 % capacity loss for over 1000 cycles [200].

Graphene-sponge-type electrodes could be used as anodes or cathodes in LIBs, with improved performance. Graphene-based hybrid materials that are thin, flexible, and stretchable and have high surface area will be applied in future electronic devices. Despite many achievements, however, new structures of graphene-based electrodes are still needed for higher performance energy-storage devices.

4.1.2 Nanosheets of 2D-TMDs for LIBs

Layered bulk-MX$_2$ has been explored for use as LIB-anode material due to its potential for improved Li-insertion and extraction. For example, MoS$_2$ has inter-layer spacing of 0.615 nm, larger than that of graphite (0.335 nm), which may easily diffuse Li ions. MoS$_2$ nanosheets have recently received great attention because of their high theoretical specific capacity (669 mAh g^{-1}), and because of a voltage for Li-ion insertion that is higher than that of graphite, which is a good anode material [201, 202]. The theoretical capacity of MoS$_2$ is two times higher than that of graphite. However, the electric conductivity of MoS$_2$ is very low, resulting in poor rate performance. One effective method for enhancing the conductivity is combining graphene, CNT, or conducting polymers with poorly conductive MoS$_2$ nanosheets. There are many reports of MoS$_2$ composites used as LIB anodes. The capacity of the MoS$_2$-rGO composite as anode was 1100 mAh g^{-1} at 100 mA g^{-1} and showed good rate capability [22]. The capacity of MoS$_2$ (66.7 %)-polyaniline nanowires

Table 4 MX_2-based anode materials for LIBs

Material	Surface area $(m^2\,g^{-1})$	Capacity $(mAh\,g^{-1})$	Cycle stability $(mAh\,g^{-1})$	References
Bulk MoS_2	4.89	800 at 0.05 A/g	226 after 50 cycles	[202]
Restacked MoS_2	9.83	800 at 0.05 A/g	750 after 50 cycles	
MoS_2 nanosheets		1062 at 1 C	907 after 50 cycles	[206]
WS_2 nanosheets		886 at 1 A/g	318.6 after 500 cycles	[205]
MoS_2-GNS(1:2)		2200 at 0.1 A/g	1290 after 50 cycles	[207]
MoS_2-rGO		1100 at 0.1 A/g		[22]
95 % MoS_2-PEO		1131 at 0.05 A/g	~900 after 50 cycles	[208]
66.7 % MoS_2-PANI NW		1063.9 at 0.1 A/g	90.2 % capacity retention after 50 cycles	[209]
Flower-like C@MoS_2	31	1419 at 0.1 A/g	80 % capacity retention after 50 cycles	[203]
MoS_2-MWCNT		1549 at 0.05 A/g	98.6 % capacity retention after 10 cycles	[210]
90 % MoS_2-G nanocable	20	1150 at 0.5 A/g reversible capacity	100 % capacity retention after 160 cycles	[204]
WS_2NT-G		996 at 0.1 A/g	500.2 after 50 cycles	[205]

(66.7 % MoS_2-PANI NW) was 952.6 mAh g^{-1} at 100 mA g^{-1}. Composites of MoS_2 (C@MoS_2) with a coating of flower-like carbon, synthesized with D-glucose and MoO_3, exhibited high reversible specific capacity (1419 mAh g^{-1} at 0.1 A g^{-1}) and good rate performance [203]. MoS_2(90 %)-graphene with a nano-cable structure exhibited a specific capacity of about 1150 mAh g^{-1} at 0.5 A g^{-1} and a long cycle life (100 % capacity retention after 160 cycles) [204]. Nano MoS_2-based composites as anode material exhibited a significant improvement in cycle performance and rate capability. WS_2 could also be a candidate material for anodes. A hybrid of 3D WS_2 nanotubes-graphene (WS_2NT-G) exhibited improved cycling stability and rate capability without additional materials. Its initial capacity was 886.1 mAh g^{-1} at 1 A g^{-1} and 318.6 mAh g^{-1} after 500 cycles [205]. Anode materials for LIBs made of 2D-MX_2 are listed in Table 4.

MoS_2 and MoS_2-graphene composites are also attractive material for novel Na-ion batteries [93, 211, 212]. Sodium-ion batteries (SIBs) have an advantage in large-scale applications that require a large amount, due to the low cost and abundance of Na. Our group worked with MoS_2 nanosheet and MoS_2-rGO composite and these materials showed high initial capacities of 254 mAh g^{-1} (MoS_2 nanosheets) and 376 mAh g^{-1} (MoS_2-rGO composite) [93]. Recently, anodes of single-layer MoS_2-carbon-nanofiber composite exhibited the best rate performance and cycling stability for Na storage in MoS_2. It achieved a specific capacity of 854 mAh g^{-1} at 0.1 A g^{-1} after 1000 cycles [213].

These results demonstrate the advantages of MX_2 nanosheets, graphene, and their hybrid composites as electrode materials for LIBs or SIBs.

4.2 Supercapacitors

Supercapacitors, another energy storage device, have advantages over batteries in their high power density and excellent cycle ability. There are two types, according to the energy storage mechanism used [214, 215]. One type is called the electrical double layer capacitors (EDLCs). They store charge in electric double layer formed at the interface between an activated electrode and an electrolyte. The others are called pseudocapacitors, and the charge storage of pseudocapacitors depends on fast faradaic redox reactions.

EDLC depends on the charge in the double layer of the electrodes used. The capacitance is given by $C = \varepsilon A/4\pi t$, where ε is the dielectric constant of the electrical double-layer region, A the electrode surface area, and t the thickness of electrical double layer. To achieve high capacitance, large specific surface area and thin double layers are necessary. Double-layer charge storage is a surface process and the surface properties of the electrode greatly influence the capacitance. Therefore, the performance of EDLCs is determined by the choice of electrode material, in relation to large surface area and high electrical conductivity. Recently, 2D layered materials (i.e., graphene, rGO, MX_2 and their composites) have been shown to be efficient, promising materials for high-performance supercapacitor electrodes due to their large surface area and large in-plane conductivity [10, 16, 216–220].

Generally, activated carbon materials have been used as electrodes for EDLCs, while transition metal chalcogenides have been investigated for use in pseudocapacitors. Thus, atomically thin graphene and $2D-MX_2$ nanosheets are attractive for use in supercapacitors.

4.2.1 Graphene Nanosheets for Supercapacitors

The capacitance of single-layer graphene was reported to be 21 mF cm^{-2}. Theoretical gravimetric capacitance of graphene materials is about 550 F g^{-1}, which is the highest capacitance value among all carbon-based electrodes [215, 221]. However, the reported capacitance of graphene-based materials is still below the theoretical value. For example, the specific capacitance of reduced graphite oxide was 135 F g^{-1} in aqueous KOH electrolyte and 99 F g^{-1} in organic electrolyte [18]. The specific capacitances of other graphene materials with different treatments were also low values (120 F g^{-1} in an organic electrolyte for a reduced graphene oxide (rGO) electrode by thermal heating [222], 282 F g^{-1} at 1 A g^{-1} for an N-doped rGO electrode) [218]. To enhance storage capacity, several groups have reported results from work on various supercapacitors using graphene-hybrid composites (e.g., graphene-CNTs composites and graphene-conductive polymer composites). There have also been many efforts to enhance capacity using porous graphene. KOH-activated rGO had large surface area (3100 m^2 g^{-1}) and specific capacitance of 165 F g^{-1} at 1.4 A g^{-1} [219]. The porous graphene grown on a

porous MgO layer gave a specific capacitance of 255 F g^{-1} at 10 mV s^{-1} in 6 M KOH aqueous solution [223]. Vertically oriented graphene showed high power density (112.6 kW kg^{-1} at 600 A g^{-1}) [10]. Restacking inhibited rGO using melamine resin exhibited high specific capacitance of 210 F g^{-1} at 0.5 A g^{-1} due to its high specific surface area (~1040 m^2 g^{-1}) and large macro pore distributions [224]. 3D macroporous embossed graphene frameworks showed both high energy (44 Wh kg^{-1}) and power densities (25 kW kg^{-1}) [225]. Recently, a supercapacitor with holey-graphene-framework electrode yielded a high capacitance (298 F g^{-1} at 1 A g^{-1}) [16].

Portable electronic devices require on-chip energy storage. Micro- or nanodevices have advantages such as small thermal time constants, high sensitivity, and integrated circuit fabrication. Micro-supercapacitor devices formed by the patterning of graphite oxide thin film exhibited good energy storage capacity and excellent cycle stability [226]. However, they also showed large internal resistance (6.5 kΩ) and poor frequency response. Recently, more than 100 micro-supercapacitors exhibited high power (200 W cm^{-3}), excellent frequency response, and were highly bendable [15]. A graphene supercapacitor using plain-woven fabric composites showed a specific capacitance of 8 mF cm^{-2} (267 F g^{-1}) [227]. This electrode had excellent flexibility, an electrode about 1–7 nm thick, and device thickness of less than 1 mm. Thus, this flexible electrode could be useful for energy storage devices in portable and wearable electronics. Although many improved electrodes for EDLC have been demonstrated, their capacitance is still not sufficient for high-performance energy storage devices.

Pseudocapacitors (another type of supercapacitor), have large specific capacitance and hybrid electrodes made of redox-active materials and highly conductive graphene-based materials. Transition metal oxides (RuO_2 and MnO_2) are widely used as pseudocapacitor electrode materials, and they use fast and reversible redox reactions for charge storage [228–230]. Graphene-38w% RuO_2 composites exhibited high specific capacitance of 570 F g^{-1} and excellent cycle stability of 97.9 % capacitance retention after 1000 cycles [229]. Graphene-MnO_2 nanoparticle composites with 3D-porous structure showed a specific capacitance of 389 F g^{-1} at 1.0 A g^{-1}, energy density of 44 Wh kg^{-1}, and power density of 25 kW kg^{-1} [225]. Micro-supercapacitor of rGO-polyaniline films showed electrochemical capacitance of 970 F g^{-1} at 2.5 A g^{-1} [230]. Cobalt oxide nanowires on 3D-graphene possessed high specific capacitance (1100 F g^{-1} at 10 A g^{-1}) [228]. Thus, hybrid graphene combined with other active materials give much higher pseudo-capacitance. Details of graphene-based supercapacitors are summarized in Table 5.

4.2.2 Nanosheets of 2D-TMDs for Supercapacitors

Nanosheets of 2D-MoS_2 have graphene-like morphology including a basal plane and an edge plane similar to graphene, which provide a large surface area. These 2D-MoS_2 nanosheets can be stacked using van der Waals interaction. The Mo atoms possess a range of oxidation states from Mo^{2+} to Mo^{6+} and show promising

Table 5 Graphene-based supercapacitors

Material	Capacitance	Electrolyte	References
EDLC			
Reduced graphite oxide	135 F/g	5.5 M KOH	[18]
	99 F/g	1 M TEA BF$_4$/AN	
rGO by thermal treatment	122 F/g at 1 A/g	1 M TEA BF$_4$/PC	[222]
N-doped rGO	282 F/g at 1 A/g	1 M TEA BF$_4$/AN	[218]
Microwave exfoliated porous rGO	165 F/g at 1.4 A/g	1 M BMIM BF$_4$/AN	[219]
Porous graphene grown on porous MgO template	255 F/g at 10 mV/s	6 M KOH	[223]
Vertically oriented graphene	156 F/g at 100 A/g	6 M KOH	[10]
3D Holey graphene	298 F/g at 1 A/g	6 M KOH	[16]
Pseudocapacitor			
rGO-RuO$_2$ composite	570 F/g at 1 A/g	1 M H$_2$SO$_4$	[229]
rGO-MnO$_2$ composite	389 F/g at 1 A/g	1 M Na$_2$SO$_4$	[225]
rGO-PANI	970 F/g at 2.5 A/g	1 M Na$_2$SO$_4$	[230]
Co$_3$O$_4$ NW on 3D graphene	1100 F/g at 10 A/g	2 M KOH	[228]

behavior as pseudocapacitors. The theoretical gravimetric capacitance of MoS$_2$ is about 1000 F g^{-1} [207]. Their performance in supercapacitors is comparable to that of CNT array electrodes. Liquid-based exfoliated 2D-MoS$_2$ nanosheets could be used as electrode materials for high-performance micro-supercapacitors. Micro-supercapacitors with finger-like electrodes using 2D-MoS$_2$ films exhibited area-specific capacitance of 8 mF cm^{-2} with excellent cycle stability [220]. Composites of MoS$_2$-polypyrrole exhibited high specific capacitance (553.7 F g^{-1} at 1 A g^{-1}) and high cycle stability [217]. Hybrid electrodes of 2D WS$_2$-rGO also exhibited high specific capacitance (350 F g^{-1}) [216]. Edge-oriented MoS$_2$-nanowall films made excellent supercapacitors [231]. Supercapacitors using 2D MX$_2$ nanosheet-graphene composites showed enhanced specific capacitance and excellent cycle stability.

Graphene and 2D-MX$_2$ nanosheets could provide electrode materials for supercapacitors to be used in portable, flexible, transparent microelectronic devices. In spite of the substantial research already done, there is still a pressing need to develop higher quality electrode materials with higher power, higher energy density, and lower cost for supercapacitor applications.

5 Summary

Today, some of the fastest growing technologies are related to electronic devices in communication, health care, and environmental monitoring. Nanomaterials that might be used to enhance energy harvesting, energy conversion, and energy

storage devices are in great demand. High-quality electrode materials are the main driving force for energy-related devices involving high power and high energy density at lower cost.

Graphene and 2D-MX$_2$ nanosheets are very attractive for energy harvesting, energy conversion and storage applications, due to their superior electrical, optical, and mechanical properties. Graphene, in particular, shown to be an ideal material for use in many of the nanoscale devices used in energy harvesting/conversion and storage applications, is still being studied for these and other energy-related purposes. Recently, 2D-MX$_2$ nanomaterials are also attracting significant attention in many energy-related applications. These 2D-MX$_2$ materials exhibit controllable bandgap properties and MX$_2$ single-layer is a direct bandgap semiconductor with bandgap energy of 1.2–2.1 eV in its elemental composition. The optical properties of 2D-MX$_2$ nanosheets have potential as energy harvesting and energy conversion materials in solar cells, photoelectrochemical cells, and photo-fuel cells. Moreover, the heterostructure of semiconducting 2D-MX$_2$ can be used to control its physical and optical properties, which include large photon absorption, high photocurrent production, and fast charge separation. Thus, atomically thin layers of 2D-MX$_2$ and graphene, with good flexibility and high transparency, are promising materials for use in future devices. In particular, 3D assembly technology will provide intrinsic advantages necessary for high efficiency in practical applications.

References

1. Novoselov KS et al (2004) Electric field effect in atomically thin carbon films. Science 306:666–669
2. Georgakilas V et al (2012) Functionalization of graphene: covalent and non-covalent approaches, derivatives and applications. Chem Rev 112:6156–6214
3. Molitor F et al (2011) Electronic properties of graphene nanostructures. J Phys: Condens Matter 23(243201):243215
4. Nair RR et al (2008) Fine structure constant defines visual transparency of graphene. Science 320:1308
5. Sarma SD et al (2011) Electronic transport in two-dimensional graphene. Rev Mod Phys 83:407–470
6. Wang QH et al (2012) Electronics and optoelectronics of two-dimensional transition metal dichalcogenides. Nat Nanotech 7:699–712
7. Zhu Y et al (2010) Graphene and graphene oxide: synthesis, properties, and applications. Adv Mater 22:3906–3924
8. Kim K et al (2014) Ultrathin organic solar cells with graphene doped by ferroelectric polarization. ACS Appl Mater Interfaces 6:3299–3304
9. Qin Jian et al (2014) Graphene networks anchored with sn@graphene as lithium ion battery anode. ACS Nano 8:1728–1738
10. Bo Z et al (2013) Vertically oriented graphene bridging active-layer/current-collector interface for ultrahigh rate supercapacitors. Adv Mater 25:5799–5806

11. Liu Z et al (2013) Package-Free flexible organic solar cells with graphene top electrodes. Adv Mater 25:4296–4301
12. Wei D et al (2013) Ultrathin rechargeable all-solid-state batteries based on monolayer graphene. J Mater Chem A 1:3177–3181
13. Zhang C et al (2013) Synthesis of amino-functionalized graphene as metal-free catalyst and exploration of the roles of various nitrogen states in oxygen reduction reaction. Nano Energy 2:88–97
14. Wang JT-W et al (2014) Low-temperature processed electron collection layers of graphene/tio$_2$ nanocomposites in thin film perovskite solar cells. Nano Lett 14:724–730
15. El-Kady MF, Kaner RB (2013) Scalable fabrication of high-power graphene micro-supercapacitors for flexible and on-chip energy storage. Nat Commun 4:1475–1484
16. Xu Y et al (2014) Holey graphene frameworks for highly efficient capacitive energy storage. Nat Commun 5:4554–4562
17. Xue Y et al (2014) Controllable synthesis of doped graphene and its applications. Small 10:2975–2991
18. Stoller MD et al (2008) Graphene-based ultracapacitors. Nano Lett 8:3498–3502
19. Wu Z-S et al (2011) Doped graphene sheets as anode materials with superhigh rate and large capacity for lithium ion batteries. ACS Nano 5:5463–5471
20. Liu C et al (2010) Graphene-based supercapacitor with an ultrahigh energy density. Nano Lett 10:4863–4868
21. Wang G et al (2009) Graphene nanosheets for enhanced lithium storage in lithium ion batteries. Carbon 47:2049–2053
22. Chhowalla M et al (2013) The chemistry of two-dimensional layered transition metal dichalcogenide nanosheets. Nat Chem 5:263–275
23. Enyashin A et al (2007) Nanosized allotropes of molybdenum disulfide. Eur Phys J Special Topics 149:103–125
24. Ataca C et al (2012) Stable, single-layer MX_2 transition-metal oxides and dichalcogenides in a honeycomb-like structure. J Phys Chem 116:8983–8999
25. Putungan DB, Kuo J-L (2014) Structural and electronic properties of monolayer 1T-MoS_2 phase, and its interaction with water adsorbed on perfect, single S-vacated and MoS_2-unit-vacated surface: density functional theory calculations. Integrated Ferroelectrics 156:93–101
26. Eda G et al (2011) Photoluminescence from chemically exfoliated MoS_2. Nano Lett 11:5111–5116
27. Yun WS et al (2012) Thickness and strain effects on electronic structures of transition metal dichalcogenides: 2H-MX_2 semiconductors (M = Mo, W; X = S, Se, Te). Phys Rev B 85:033305
28. Kuc A et al (2011) Influence of quantum confinement on the electronic structure of the transition metal sulfide TS_2. Phys Rev B 83:245213
29. Kadantsev ES, Hawrylakb P (2012) Electronic structure of a single MoS_2 monolayer. Solid State Comm 152:909–913
30. Huang W et al (2014) Theoretical study of thermoelectric properties of few-layer MoS_2 and WSe_2. Phys Chem Chem Phys 16:10866–10874
31. Kumara A, Ahluwalia PK (2012) Electronic structure of transition metal dichalcogenides monolayers 1H-MX_2 (M = Mo, W; X = S, Se, Te) from ab-initio theory: new direct band gap semiconductors. Eur Phys J B 85:186–193
32. Radisavljevic B et al (2011) Single-layer MoS_2 transistors. Nat Nanotech 6:147–150
33. Bertolazzi S et al (2011) Stretching and breaking of ultrathin MoS_2. ACS Nano 5:9703–9709
34. Ayari A et al (2007) Realization and electrical characterization of ultrathin crystals of layered transition-metal dichalcogenides. J Appl Phys 101:014057
35. Zhan Y et al (2012) Large-area vapor-phase growth and characterization of MoS_2 atomic layers on a SiO_2 substrate. Small 8:966–971
36. Zeng H et al (2012) Valley polarization in MoS_2 monolayers by optical pumping. Nat Nanotech 7:490–493

37. Mak KF et al (2012) Control of valley polarization in monolayer MoS_2 by optical helicity. Nat Nanotech 7:494–498
38. Yue Q et al (2012) Mechanical and electronic properties of monolayer MoS_2 under elastic strain. Phys Lett A 376:1166–1170
39. Zhou M et al (2014) Production of graphene by liquid-phase exfoliation of intercalated graphite. Int J Electrochem Sci 9:810–820
40. Bonaccorso F et al (2012) Production and processing of graphene and 2d crystals. Mater Today 15:564–589
41. Allen MJ et al (2010) Honeycomb carbon: a review of graphene. Chem Rev 110:132–145
42. Kumar P et al (2013) Graphene: synthesis, properties and application in transparent electronic devices. Rev Adv Sci Eng 2:1–21
43. Park S, Ruoff RS (2009) Chemical methods for the production of graphenes. Nat Nanotech 4:217–224
44. Kim KS et al (2009) Large-scale pattern growth of graphene films for stretchable transparent electrodes. Nature 457:706–710
45. Shen Y, Lua AC (2013) A facile method for the large-scale continuous synthesis of graphene sheets using a novel catalyst. Sci Rep 3:3037–3042
46. Zhou H et al (2013) Chemical vapour deposition growth of large single crystals of monolayer and bilayer graphene. Nat Commun 4:2096–2103
47. Lee J-H et al (2014) Wafer-scale growth of single-crystal monolayer graphene on reusable hydrogen-terminated germanium. Science 344(6181):286–289
48. Muñoz R, Gómez-Aleixandre C (2013) Review of CVD synthesis of graphene. Chem Vap Depos 19:297–322
49. Novoselov KS et al (2005) Two-dimensional atomic crystals. Proc Natl Acad Sci USA 102:10451–10453
50. Li H et al (2012) Fabrication of single- and multilayer MoS_2 film-based field-effect transistors for sensing no at room temperature. Small 8:63–67
51. Osada M, Sasaki T (2012) Two-dimensional dielectric nanosheets: novel nanoelectronics from nanocrystal building blocks. Adv Mater 24:210–228
52. Kalantar-zadeh K et al (2010) Synthesis of atomically thin WO_3 sheets from hydrated tungsten trioxide. Chem Mater 22:5660–5666
53. Late DJ et al (2012) Hysteresis in single-layer MoS_2 field effect transistors. ACS Nano 6:5635–5641
54. Lee C et al (2010) Anomalous lattice vibrations of single- and few-layer MoS_2. ACS Nano 4:2695–2700
55. McDonnell S et al (2013) HfO_2 on MoS_2 by atomic layer deposition: adsorption mechanisms and thickness scalability. ACS Nano 7:10354–10361
56. Radisavljevic B et al (2011) Integrated circuits and logic operations based on single-layer MoS_2. ACS Nano 5:9934–9938
57. Bao W et al (2013) High mobility ambipolar MoS_2 field-effect transistors: substrate and dielectric effects. Appl Phys Lett 102:042104
58. Splendiani A et al (2010) Emerging photoluminescence in monolayer MoS_2. Nano Lett 10:1271–1275
59. Sun Y et al (2014) Probing local strain at MX_2—metal boundaries with surface plasmon-enhanced raman scattering. Nano Lett 14:5329–5334
60. Zhang Y et al (2012) Ambipolar MoS_2 thin flake transistors. Nano Lett 12:1136–1140
61. Mak KF et al (2010) Atomically thin MoS_2: a new direct-gap semiconductor. Phys Rev Lett 105:136805
62. Zhang Y et al (2013) Review of chemical vapor deposition of graphene and related applications. Acc Chem Res 46:2329–2339
63. Gong Y et al (2013) Stabilizing nanostructured solid oxide fuel cell cathode with atomic layer deposition. Nano Lett 13:4340–4345
64. Lee Y-H et al (2012) Synthesis of large-area mos2 atomic layers with chemical vapor deposition. Adv Mater 24:2320–2325

65. Lin Y-C et al (2012) Wafer-scale MoS_2 thin layers prepared by MoO_3 sulfurization. Nanoscale 4:6637–6641

66. Zande AMvd et al (2013) Grains and grain boundaries in highly crystalline monolayer molybdenum disulphide. Nature Mater 12:554–561

67. Wang X et al (2013) Controlled synthesis of highly crystalline MoS_2 flakes by chemical vapor deposition. J Am Chem Soc 135:5304–5307

68. Najmaei S et al (2013) Vapour phase growth and grain boundary structure of molybdenum disulphide atomic layers. Nat Mater 12:754–759

69. Lee Y-H et al (2013) Synthesis and transfer of single-layer transition metal disulfides on diverse surfaces. Nano Lett 13:1852–1857

70. Liu K-K et al (2012) Growth of large-area and highly crystalline MoS_2 thin layers on insulating substrates. Nano Lett 12:1538–1544

71. Chang Y-H et al (2014) Monolayer $MoSe_2$ grown by chemical vapordeposition for fast photodetection. ACS Nano 8:8582–8590

72. Huang J-K et al (2014) Large-area synthesis of highly crystalline WSe_2 monolayers and device applications. ACS Nano 8:923–930

73. Shim GW et al (2014) Large-area single-layer $MoSe_2$ and Its van der waals heterostructures. ACS Nano 8:6655–6662

74. Zhang Y et al (2013) Controlled growth of high-quality monolayer WS_2 layers on sapphire and imaging its grain boundary. ACS Nano 7:8963–8971

75. Ji Q et al (2013) Epitaxial monolayer MoS_2 on mica with novel photoluminescence. Nano Lett 13:3870–3877

76. Yu Y et al (2013) Controlled scalable synthesis of uniform, high-quality monolayer and few-layer MoS_2 films. Sci Rep 3:1866–1871

77. Cong C et al (2014) Synthesis and optical properties of large-area single-crystalline 2d semiconductor WS_2 monolayer from chemical vapor deposition. Adv Optical Mater 2:131–136

78. Cai M et al (2012) Methods of graphite exfoliation. J Mater Chem 22:24992–25002

79. Park KH et al (2012) Exfoliation of non-oxidized graphene flakes for scalable conductive film. Nano Lett 12:2871–2876

80. Tung VC et al (2009) High-throughput solution processing of large-scale graphene. Nat Nanotech 4:25–29

81. Eda G, Chhowalla M (2010) Chemically derived graphene oxide: towards large-area thin-film electronics and optoelectronics. Adv Mater 22:2392–2415

82. Wei D, Liu Y (2010) Controllable synthesis of graphene and its applications. Adv Mater 22:3225–3241

83. Dreyer DR et al (2010) The chemistry of graphene oxide. Chem Soc Rev 39:228–240

84. Gao W et al (2009) New insights into the structure and reduction of graphite oxide. Nat Chem 1:403–408

85. Dikin DA et al (2007) Preparation and characterization of graphene oxide paper. Nat 448:457–460

86. Sundaram RS et al (2008) Electrochemical modification of graphene. Adv Mater 20:3050–3053

87. Stankovicha S et al (2007) Synthesis of graphene-based nanosheets via chemical reduction of exfoliated graphite oxide. Carbon 45:1558–1565

88. Zhou M et al (2009) Controlled synthesis of large-area and patterned electrochemically reduced graphene oxide films. Chem Eur J 15:6116–6120

89. McAllister MJ et al (2007) Single sheet functionalized graphene by oxidation and thermal expansion of graphite. Chem Mater 19:4396–4404

90. Yang D et al (2009) Chemical analysis of graphene oxide films after heat and chemical treatments by X-ray photoelectron and micro-raman spectroscopy. Carbon 47:145–152

91. Shao Y et al (2010) Facile and controllable electrochemical reduction of graphene oxide and its applications. J Mater Chem 20:743–748

92. Hernandez Y et al (2008) High-yield production of graphene by liquid-phase exfoliation of graphite. Nat Nanotech 3:563–568

93. Bang GS et al (2014) Effective liquid-phase exfoliation and sodium ion battery application of MoS$_2$ nanosheets. ACS Appl Mater Interfaces 6:7084–7089

94. Cunningham G et al (2012) Solvent exfoliation of transition metal dichalcogenides: dispersibility of exfoliated nanosheets varies only weakly between compounds. ACS Nano 6:3468–3480

95. Zhou K-G et al (2011) A mixed-solvent strategy for efficient exfoliation of inorganic graphene analogues. Angew Chem Int Ed 50:10839–10842

96. Coleman JN et al (2011) Two-dimensional nanosheets produced by liquid exfoliation of layered materials. Science 331:568–571

97. Smith RJ et al (2011) Large-scale exfoliation of inorganic layered compounds in aqueous surfactant solutions. Adv Mater 23:3944–3948

98. Zeng Z et al (2011) Single-layer semiconducting nanosheets: high-yield preparation and device fabrication. Angew Chem Int Ed 50:11093–11097

99. Wang H et al (2013) Electrochemical tuning of vertically aligned MoS$_2$ nanofilms and its application in improving hydrogen evolution reaction. Proc Natl Acad Sci USA 110:19701–19706

100. De S, Coleman JN (2010) Are there fundamental limitations on the sheet resistance and transmittance of thin graphene films? ACS Nano 4:2713–2720

101. Bae S et al (2010) Roll-to-roll production of 30-inch graphene films for transparent electrodes. Nat Nanotech 5:574–578

102. Zhu Y et al (2011) Rational design of hybrid graphene films for high-performance transparent electrodes. ACS Nano 5:6472–6479

103. Wang X et al (2008) Transparent, conductive graphene electrodes for dye-sensitized solar cells. Nano Lett 8:323–327

104. Li S-S et al (2010) Solution-processable graphene oxide as an efficient hole transport layer in polymer solar cells. ACS Nano 4:3169–3174

105. DeArco LG et al (2010) Continuous, highly flexible, and transparent graphene films by chemical vapor deposition for organic photovoltaics. ACS Nano 4:2865–2873

106. Hsu C-L et al (2012) Layer-by-layer graphene/TCNQ stacked films as conducting anodes for organic solar cells. ACS Nano 6:5031–5039

107. Gong F et al (2013) Enhanced charge transportation in a polypyrrole counter electrode via incorporation of reduced graphene oxide sheets for dye-sensitized solar cells. Phys Chem Chem Phys 15:546–552

108. Chen L et al (2013) Graphene quantum-dot-doped polypyrrole counter electrode for high-performance dye-sensitized solar cells. ACS Appl Mater Interfaces 5:2047–2052

109. Peng J et al (2012) Graphene quantum dots derived from carbon fibers. Nano Lett 12:844–849

110. Zhang Y et al (2013) Graphene quantum dots/gold electrode and its application in living cell H$_2$O$_2$ detection. Nanoscale 5:1816–1819

111. Yan X et al (2010) Large, solution-processable graphene quantum dots as light absorbers for photovoltaics. Nano Lett 10:1869–1873

112. Zhang Y et al (2012) Graphene transforms wide band gap zns to a visible light photocatalyst. the new role of graphene as a macromolecular photosensitizer. ACS Nano 6:9777–9789

113. Williams KJ et al (2013) Hot electron injection from graphene quantum dots to TiO$_2$. ACS Nano 7:1388–1394

114. Miao X et al (2012) High efficiency graphene solar cells by chemical doping. Nano Lett 12:2745–2750

115. Song J et al (2011) Enhancement of photogenerated electron transport in dye-sensitized solar cells with introduction of a reduced graphene oxide-TiO$_2$ junction. Chem Eur J 17:10832–10837

116. Liu J et al (2012) Hole and electron extraction layers based on graphene oxide derivatives for high-performance bulk heterojunction solar cells. Adv Mater 24:2228–2233

117. Bernardi M et al (2013) Extraordinary sunlight absorption and one nanometer thick photovoltaics using two-dimensional monolayer materials. Nano Lett 13:3664–3670

118. Wu M et al (2011) Economical and effective sulfide catalysts for dye-sensitized solar cells as counter electrodes. Phys Chem Chem Phys 13:19298–19301
119. Patil SA et al (2014) Highly efficient and stable DSSCs of wet-chemically synthesized MoS_2 counter electrode. Dalton Trans 43:5256–5259
120. Lee LTL et al (2014) Few-layer $MoSe_2$ possessing high catalytic activity towards iodide/tri-iodide redox shuttles. Sci Rep 4:4063–4069
121. Yue G et al (2012) A catalytic composite film of MoS_2/graphene flake as a counter electrode for Pt-free dye-sensitized solar cells. Electrochim Acta 85:162–168
122. Liu C-J et al (2012) Facile synthesis of MoS_2/graphene nanocomposite with high catalytic activity toward triiodide reduction in dye-sensitized solar cells. J Mater Chem 22:21057–21064
123. Shanmugam M et al (2012) Layered semiconductor molybdenum disulfide nanomembrane based Schottky-barrier solar cells. Nanoscale 4:7399–7405
124. Shanmugam M et al (2012) Molybdenum disulphide/titanium dioxide nanocomposite-poly 3-hexylthiophene bulk heterojunction solar cell. Appl Phys Lett 100:153901
125. Yun J-M et al (2013) Efficient work-function engineering of solutionprocessed MoS_2 thin-films for novel hole and electron transport layers leading to high-performance polymer solar cells. J Mater Chem C 1:3777–3783
126. Gu X et al (2013) A solution-processed hole extraction layer made from ultrathin MoS_2 nanosheets for effi cient organic solar cells. Adv Energy Mater 3:1262–1268
127. Niu L et al (2014) Salt-assisted high-throughput synthesis of single- and few-layer transition metal dichalcogenides and their application in organic. Solar Cells. small. doi:10.1002/smll.201401647
128. Yun J-M et al (2014) Exfoliated and partially oxidized MoS_2 nanosheets by one-pot reaction for efficient and stable organic solar cells. Small 10:2319–2324
129. Yang X et al (2014) Au nanoparticles on ultrathin MoS_2 sheets for plasmonic organic solar cells. J Mater Chem A 2:14798–14806
130. Geim AK, Grigorieva IV (2013) Van der Waals heterostructures. Nature 499:419–425
131. Haigh SJ et al (2012) Cross-sectional imaging of individual layers and buried interfaces of graphene-based heterostructures and superlattices. Nat Mater 11:764–767
132. Lopez-Sanchez O et al (2014) Light generation and harvesting in a van der waals heterostructure. ACS Nano 8:3042–3048
133. Hong X et al (2014) Ultrafast charge transfer in atomically thin MoS_2/WS_2 heterostructures. Nat Nanotech 9:682–686
134. Lee C-H et al (2014) Atomically thin p-n junctions with van der Waals heterointerfaces. Nat Nanotech 9:676–681
135. Britnell L et al (2013) Strong light-matter interactions in heterostructures of atomically thin films. Science 340:1311–1314
136. Arico AS et al (2005) Nanostructured materials for advanced energy conversion and storage devices. Nat Mater 4:366–377
137. Shao Y et al (2010) Nitrogen-doped graphene and its electrochemical applications. J Mater Chem 20:7491–7496
138. Li Y et al (2012) Stabilization of high-performance oxygen reduction reaction pt electrocatalyst supported on reduced graphene oxide/carbon black composite. J Am Chem Soc 134:12326–12329
139. Wang C et al (2013) A unique platinum-graphene hybrid structure for high activity and durability in oxygen reduction reaction. Sci Rep 3:2580–2586
140. Qu L et al (2010) Nitrogen-doped graphene as efficient metal-free electrocatalyst for oxygen reduction in fuel cells. ACS Nano 4:1321–1326
141. Yang Z et al (2012) Sulfur-doped graphene as an efficient metal-free cathode catalyst for oxygen reduction. ACS Nano 6:205–211

142. Li Q et al (2012) Nitrogen-doped colloidal graphene quantum dots and their size-dependent electrocatalytic activity for the oxygen reduction reaction. J Am Chem Soc 134:18932–18935
143. Li Y et al (2010) Catalytic performance of Pt nanoparticles on reduced graphene oxide for methanol electro-oxidation. Carbon 48:1124–1130
144. Zhou Y-G et al (2010) A facile approach to the synthesis of highly electroactive Pt nano-particles on graphene as an anode catalyst for direct methanol fuel cells. Chem Commun 46:5951–5953
145. Li Y et al (2009) Preparation and electrochemical performance for methanol oxidation of pt/graphene nanocomposites. Electrochem Commun 11:846–849
146. Kakaei K, Zhiani M (2013) A new method for manufacturing graphene and electrochemical characteristic of graphene-supported Pt nanoparticles in methanol oxidation. J Power Sour 225:356–363
147. Xin Y et al (2011) Preparation and characterization of Pt supported on graphene with enhanced electrocatalytic activity in fuel cell. J Power Sour 196:1012–1018
148. Maiyalagan T et al (2012) Electrodeposited Pt on three-dimensional interconnected gra-phene as a free-standing electrode for fuel cell application. J Mater Chem 22:5286–5290
149. Yoo E et al (2011) Sub-nano-Pt cluster supported on graphene nanosheets for CO tolerant catalysts in polymer electrolyte fuel cells. J Power Sour 196:110–115
150. Wang H et al (2012) Review on recent progress in nitrogen-doped graphene: synthesis, characterization, and its potential applications. ACS Catal 2:781–794
151. Sheng Z-H et al (2011) Catalyst-free synthesis of nitrogen-doped graphene via ther-mal annealing graphite oxide with melamine and its excellent electrocatalysis. ACS Nano 5:4350–4358
152. Wang S et al (2011) Polyelectrolyte-functionalized graphene as metal-free electrocatalysts for oxygen reduction. ACS Nano 5:6202–6209
153. Lin Z et al (2012) Facile synthesis of nitrogen-doped graphene via pyrolysis of graphene oxide and urea, and its electrocatalytic activity toward the oxygen-reduction reaction. Adv Energy Mater 2:884–888
154. Zhao Y et al (2012) A versatile, ultralight, nitrogen-doped graphene framework. Angew Chem Int Ed 51:11371–11375
155. Lee KR et al (2010) Electrochemical oxygen reduction on nitrogen doped graphene sheets in acid media. Electrochem Commun 12:1052–1055
156. Ahmed MS, Jeon S (2012) New functionalized graphene sheets for enhanced oxygen reduc-tion as metal-free cathode electrocatalysts. J Power Sour 218:168–173
157. Wu J et al (2013) Electrocatalytic activity of nitrogen-doped graphene synthesized via a one-pot hydrothermal process towards oxygen reduction reaction. J Power Sour 227:185–190
158. Yang Z et al (2013) Recent progress in doped carbon nanomaterials as effective cathode catalysts for fuel cell oxygen reduction reaction. J Power Sour 236:238–249
159. Jafri RI et al (2010) Nitrogen doped graphene nanoplatelets as catalyst support for oxygen reduction reaction in proton exchange membrane fuel cell. J Mater Chem 20:7114–7117
160. He C et al (2013) A strategy for mass production of self-assembled nitrogen-doped gra-phene as catalytic materials. J Mater Chem A 1:1401–1406
161. Zhang L et al (2012) Effect of microstructure of nitrogen-doped graphene on oxygen reduc-tion activity in fuel cells. Langmuir 28:7542–7550
162. Leger J-M (2001) Mechanistic aspects of methanol oxidation on platinum-based electrocat-alysts. J Appl Electrochem 31:767–771
163. Yoo E et al (2011) Sub-nano-Pt cluster supported on graphene nanosheets for CO tolerant catalysts in polymer electrolyte fuel cells. J Power Sour 196:110–115
164. Zhao Y et al (2011) Enhanced electrocatalytic oxidation of methanol on Pd/polypyrrole-gra-phene in alkaline medium. Electrochim Acta 56:1967–1972

165. Yoo E et al (2009) Enhanced electrocatalytic activity of pt subnanoclusters on graphene nanosheet surface. Nano Lett 9:2255–2259
166. Yang X et al (2012) Bimetallic PtPd nanoparticles on Nafion–graphene film as catalyst for ethanol electro-oxidation. J Mater Chem 22:8057–8062
167. Chen X et al (2011) Synthesis of "Clean" and well-dispersive Pd nanoparticles with excellent electrocatalytic property on graphene oxide. J Am Chem Soc 133:3693–3695
168. Zhao H et al (2011) Fabrication of a palladium nanoparticle/graphene nanosheet hybrid via sacrifice of a copper template and its application in catalytic oxidation of formic acid. Chem Commun 47:2014–2016
169. Rao CV et al (2011) Graphene-supported ptau alloy nanoparticles: a highly efficient anode for direct formic acid fuel cells. J Phys Chem C 115:21963–21970
170. Hinnemann B et al (2005) Biomimetic hydrogen evolution: MoS_2 nanoparticles as catalyst for hydrogen evolution. J Am Chem Soc 127:5308–5309
171. Kibsgaard J et al (2012) Engineering the surface structure of MoS_2 to preferentially expose active edge sites for electrocatalysis. Nat Mater 11:963–969
172. Jaramillo TF et al (2007) Identification of active edge sites for electrochemical H_2 evolution from MoS_2 nanocatalysts. Science 317:100–103
173. Lauritsen JV et al (2004) Atomic-scale insight into structure and morphology changes of MoS_2 nanoclusters in hydrotreating catalysts. J Catal 221:510–522
174. Bonde J et al (2009) Hydrogen evolution on nano-particulate transition metal sulfides. Faraday Discuss 140:219–231
175. Benck JD et al (2012) Amorphous molybdenum sulfide catalysts for electrochemical hydrogen production: insights into the origin of their catalytic activity. ACS Catal 2:1916–1923
176. Xie J et al (2013) Defect-rich MoS_2 ultrathin nanosheets with additional active edge sites for enhanced electrocatalytic hydrogen evolution. Adv Mater 25:5807–5813
177. Merki D et al (2011) Amorphous molybdenum sulfide films as catalysts for electrochemical hydrogen production in water. Chem Sci 2:1262–1267
178. Wang H et al (2014) Electrochemical tuning of MoS_2 nanoparticles on three-dimensional substrate for efficient hydrogen evolution. ACS Nano 8:4940–4947
179. Voiry D et al (2013) Enhanced catalytic activity in strained chemically exfoliated WS_2 nanosheets for hydrogen evolution. Nat Mater 12:850–855
180. Liao L et al (2013) MoS_2 formed on mesoporous graphene as a highly active catalyst for hydrogen evolution. Adv Funct Mater 23:5326–5333
181. Li Y et al (2011) MoS_2 nanoparticles grown on graphene: an advanced catalyst for the hydrogen evolution reaction. J Am Chem Soc 133:7296–7299
182. Kim J et al (2013) Enhanced electrocatalytic properties of transition-metal dichalcogenides sheets by spontaneous gold nanoparticle decoration. J Phys Chem Lett 4:1227–1232
183. Huang X et al (2013) Solution-phase epitaxial growth of noble metal nanostructures on dispersible single-layer molybdenum disulfide nanosheets. Nat Commun 4:1444–1451
184. Yuwen L et al (2014) General synthesis of noble metal (Au, Ag, Pd, Pt) nanocrystal modified MoS_2 nanosheets and the enhanced catalytic activity of $Pd-MoS_2$ for methanol oxidation. Nanoscale 6:5762–5769
185. Lukowski MA et al (2013) Enhanced hydrogen evolution catalysis from chemically exfoliated metallic MoS_2 nanosheets. J Am Chem Soc 135:10274–10277
186. Voiry D et al (2013) Conducting MoS_2 nanosheets as catalysts for hydrogen evolution reaction. Nano Lett 13:6222–6227
187. Yang J et al (2013) Two-dimensional hybrid nanosheets of tungsten disulfide and reduced graphene oxide as catalysts for enhanced hydrogen evolution. Angew Chem Int Ed 52:13751–13754
188. Yin Z et al (2014) Au nanoparticle-modified MoS_2 nanosheet-based photoelectrochemical cells for water splitting. Small 10:3537–3543
189. Tarascon JM, Armand M (2001) Issues and challenges facing rechargeable lithium batteries. Nature 414:359–367

190. Lian P et al (2010) Large reversible capacity of high quality graphene sheets as an anode material for lithium-ion batteries. Electrochim Acta 55:3909–3914
191. Zhou X, Liu Z (2011) Graphene foam as an anode for high-rate Li-ion batteries. IOP Conf Series: Mater Sci Eng 18:062006
192. Fang Y et al (2013) Two-dimensional mesoporous carbon nanosheets and their derived graphene nanosheets: synthesis and efficient lithium ion storage. J Am Chem Soc 135:1524–1530
193. Zhu X et al (2011) Nanostructured reduced graphene oxide/Fe_2O_3 composite as a high-performance anode material for lithium ion batteries. ACS Nano 5:3333–3338
194. Yin S et al (2011) Assembly of graphene sheets into hierarchical structures for high-performance energy storage. ACS Nano 5:3831–3838
195. Zhou X et al (2012) Self-assembled nanocomposite of silicon nanoparticles encapsulated in graphene through electrostatic attraction for lithium-ion batteries. Adv Energy Mater 2:1086–1090
196. Wang B et al (2013) Adaptable siliconcarbon nanocables sandwiched between reduced graphene oxide sheets as lithium ion battery anodes. ACS Nano 7:1437–1445
197. Wang C et al (2009) Electrochemical properties of graphene paper electrodes used in lithium batteries. Chem Mater 21:2604–2606
198. Ning G et al (2013) Chemical vapor deposition derived flexible graphene paper and its application as high performance anodes for lithium rechargeable batteries. J Mater Chem A 1:408–414
199. Li N et al (2012) Flexible graphene-based lithium ion batteries with ultrafast charge and discharge rates. Proc Natl Acad Sci USA 109:17360–17365
200. Yang S et al (2013) Bottom-up approach toward single-crystalline VO_2-graphene ribbons as cathodes for ultrafast lithium storage. Nano Lett 13:1596–1601
201. J-w Seo et al (2007) Two-dimensional nanosheet crystals. Angew Chem Int Ed 46:8828–8831
202. Du G et al (2010) Superior stability and high capacity of restacked molybdenum disulfide as anode material for lithium ion batteries. Chem Commun 46:1106–1108
203. Hu S et al (2014) Preparation of carbon coated MoS_2 flower-like nanostructure with self-assembled nanosheets as high-performance lithium-ion battery anodes. J Mater Chem A 2:7862–7872
204. Kong D et al (2014) Rational design of MoS_2@graphene nanocables: towards high performance electrode materials for lithium ion batteries. Energy Environ Sci 7:3320–3325
205. Chen R et al (2014) Free-standing hierarchically sandwich-type tungsten disulfide nanotubes/graphene anode for lithium-ion batteries. Nano Lett 14:5899–5904
206. Hwang H et al (2011) MoS_2 nanoplates consisting of disordered graphene-like layers for high rate lithium battery anode materials. Nano Lett 11:4826–4830
207. Chang K, Chen W (2011) In situ synthesis of MoS_2/Graphene nanosheet composites with extraordinarily high electrochemical performance for lithium ion batteries. Chem Commun 47:4252–4254
208. Xiao J et al (2010) Exfoliated MoS_2 nanocomposite as an anode material for lithium ion batteries. Chem Mater 22:4522–4524
209. Yang L et al (2013) Hierarchical MoS_2/Polyaniline nanowires with excellent electrochemical performance for lithium-ion batteries. Adv Mater 25:1180–1184
210. Shi Y et al (2013) Self-assembly of hierarchical MoSx/CNT nanocomposites (2, x,3): towards high performance anode materials for lithium ion batteries. Sci Rep 3:2169–2176
211. David L et al (2014) MoS_2/Graphene composite paper for sodium-ion battery electrodes. ACS Nano 8:1759–1770
212. Park J et al (2013) Discharge mechanism of MoS_2 for sodium ion battery: Electrochemical measurements and characterization. Electrochim Acta 92:427–432
213. Zhu C et al (2014) Single-layered ultrasmall nanoplates of mos_2 embedded in carbon nanofibers with excellent electrochemical performance for lithium and sodium storage. Angew Chem Int Ed 53:2152–2156

214. Simon P, Gogotsi Y (2008) Materials for electrochemical capacitors. Nat Mater 7:845–854
215. Conway BE et al (1997) The role and utilization of pseudocapacitance for energy storage by supercapacitors. J Power Sour 66:1–14
216. Ratha S, Rout CS (2013) Supercapacitor electrodes based on layered tungsten disulfide-reduced graphene oxide hybrids synthesized by a facile hydrothermal method. ACS Appl Mater Interfaces 5:11427–11433
217. Ma G et al (2013) In situ intercalative polymerization of pyrrole in graphene analogue of MoS_2 as advanced electrode material in supercapacitor. J Power Sour 229:72–78
218. Jeong HM et al (2011) Nitrogen-doped graphene for high-performance ultracapacitors and the importance of nitrogen-doped sites at basal planes. Nano Lett 11:2472–2477
219. Zhu Y et al (2011) Carbon-based supercapacitors produced by activation of graphene. Science 332:1537–1541
220. Cao L et al (2013) Direct laser-patterned micro-supercapacitors from paintable MoS_2 films. Small 9:2905–2910
221. Xia J et al (2009) Measurement of the quantum capacitance of graphene. Nat Nanotech 4:505–509
222. Zhu Y et al (2010) Exfoliation of graphite oxide in propylene carbonate and thermal reduction of the resulting graphene oxide platelets. ACS Nano 4:1227–1233
223. Ning G et al (2011) Gram-scale synthesis of nanomesh graphene with high surface area and its application in supercapacitor electrodes. Chem Commun 47:5976–5978
224. Lee JH et al (2013) Restacking-inhibited 3D reduced graphene oxide for high performance supercapacitor electrodes. ACS Nano 7:9366–9374
225. Choi BG et al (2012) 3D macroporous graphene frameworks for supercapacitors with high energy and power densities. ACS Nano 6:4020–4028
226. Gao W et al (2011) Direct laser writing of micro-supercapacitors on hydrated graphite oxide films. Nat Nanotech 6:496–500
227. Zang X et al (2014) Highly flexible and adaptable, all-solid-state supercapacitors based on graphene woven-fabric film electrodes. Small 10:2583–2588
228. Dong X-C et al (2012) 3D graphene-cobalt oxide electrode for high-performance supercapacitor and enzymeless glucose detection. ACS Nano 6:3206–3213
229. Wu Z-S et al (2010) Anchoring hydrous RuO_2 on graphene sheets for high-performance electrochemical capacitors. Adv Funct Mater 20:3595–3602
230. Xue M et al (2012) Structure-based enhanced capacitance. in situ growth of highly ordered polyaniline nanorods on reduced graphene oxide patterns. Adv Funct Mater 22:1284–1290
231. Soon JM, Loh KP (2007) Electrochemical double-layer capacitance of MoS_2 nanowall films. Electrochem Solid-State Lett 10:A250–A254